

High Precision Measurement of the Proton Charge Radius

A. Gasparian (spokesperson and contact person), R. Pedroni, Z. Ahmed
North Carolina A&T State University, Greensboro, NC 27411

M. Khandaker (co-spokesperson), V. Punjabi, C. Salgado
Norfolk State University, Norfolk, VA 23504

I. Akushevich, H. Gao (co-spokesperson), M. Huang, S. Jawalkar,
G. Laskaris, S. Malace, M. Meziane, C. Peng, Q.J. Ye, X.F. Yan, Y. Zhang
Duke University, Durham, NC 27708

A. Deur, E. Pasyuk, S. Stepanyan, V. Kubarovsky,
D. Gaskell, M. Jones, D. Lawrence, S. Taylor, B. Wojtsekhowski, B. Zihlmann
Thomas Jefferson National Accelerator Facility, Newport News, VA 23606

J. Dunne, D. Dutta (co-spokesperson), A. Narayan, L. Ndukum,
M. Shabestari, A. Subedi, L. Ye
Mississippi State University, Mississippi State, MS 39762

L. Gan
University of North Carolina Wilmington, Wilmington, NC 28403

G. Gavalian
Old Dominion University, Norfolk, VA 23529

C.F. Perdrisat
College of William & Mary, Williamsburg, VA 23185

A. Afanasev
The George Washington University, Washington, DC 20052

C. Crawford
University of Kentucky, Lexington, KY 40506

May 4, 2012

Abstract

We propose to perform a high precision ep elastic cross sections measurement at very low four-momentum transfer squared, Q^2 , from 10^{-4} to 10^{-2} $(\text{GeV}/c)^2$ range using a high resolution calorimeter. The absolute value of the ep cross sections will be controlled by a well known QED process, the Møller scattering, which will be continuously measured in this experiment within similar kinematics and the same experimental acceptances. The high precision differential cross sections, measured for the first time in this low Q^2 range, will allow a sub-percent and essentially model independent extraction of the proton charge radius. With that, this experiment will have a direct impact on the “*proton charge radius crisis*” currently developing in hadronic and atomic physics. We propose to perform this experiment in Hall B at Jefferson Lab using the unique low-intensity electron beam control capabilities of the hall and part of the PrimEx-II infrastructure.

Contents

1	PAC 38 comments	1
2	Summary of updates to the PAC38 proposal	1
3	Windowless cryo-cooled hydrogen gas flow target	2
3.1	Target cell	4
3.2	Target cooling system	4
3.3	Target pumping system	5
3.4	Target gas handling system	6
3.5	Target vacuum chambers	7
3.6	Beamline integration of the target	7
4	Beam halo studies in Hall-B	9
5	Radiative corrections extended to Q^2 of 10^{-4} GeV²	12
5.1	Radiative corrections to ep elastic scattering beyond the URA	12
5.2	Radiative corrections to Møller scattering	13
6	Monte Carlo simulation of the experimental background	16
6.1	Geometry	16
6.2	Physics processes	16
6.3	Event generator for beam halo	16
6.4	Simulation results	17
7	Simulation of the effect of radiative corrections on the extraction of $\langle r_p \rangle$	20
8	Summary	21
	References	22
	Appendices	23
A	Expressions for radiative corrections beyond the URA	23
B	Original proposal PR12-11-106 for PAC38, August 22, 2011	25

1 PAC 38 comments

The PAC38 conditionally approved the proposed “High Precision Measurement of the Proton Charge Radius” (PR12-11-106) with the following comments:

“The proponents hope to resolve the “proton charge radius crisis” stemming from a 6-sigma discrepancy between a new measurement of the Lamb shift in muonic hydrogen and existing data ... Testing of this result is among the most timely and important measurements in physics.”

“... This is a novel technique that should be able to achieve the required precision.”

“Before the proposal can be approved and beam time assigned, the PAC would need to see more careful modeling related to beam halo with the exact target geometry proposed and all sources of background included. Until a realistic and final target design is completed, the beam requirements cannot be firmly established and matched to expected accelerator performance. In addition, the PAC was not convinced that all Coulomb effects were properly included in the simulations presented. The proponents will also need to demonstrate that they have a path to extend radiative corrections to 10^{-4} GeV^2 with the required precision.”

2 Summary of updates to the PAC38 proposal

The following is a summary of updates to the proposal (PR12-11-106) addressing all the concerns of PAC38.

- A complete design of the target is presented in Section 3. The target cell has been redesigned to alleviate some of the sensitivity to beam halo and a cryo-cooler has been added to help achieve the high density in the target cell. We have submitted a MRI proposal to the NSF to build the target.
- Beam halo studies in Hall B (Section 4).
- Radiative corrections to Q^2 down to 10^{-4} GeV^2 (Section 5).
- Background simulation studies (Section 6).
- Extraction of $\langle r_p \rangle$ with effect of radiative corrections (Section 7).

3 Windowless cryo-cooled hydrogen gas flow target

The design and engineering of polarized or unpolarized internal gas flow targets are well established and understood. Indeed, such targets have been used in different successful experiments. The 40 cm long polarized ^3He target installed in the HERA positron beam during the HERMES experiment [1] reached values of thickness up to 6×10^{15} atoms/cm². Another example, the 60 cm long deuterium/hydrogen polarized internal gas target built for the BLAST experiment [2] attained a thickness of 7×10^{13} atoms/cm² where polarized atoms were injected into a thin-walled storage cell by an Atomic Beam Source. On the other hand, the 27 cm long unpolarized OLYMPUS target [3], whose design is based on the HERMES and BLAST experiments, is cooled to 25 K and has a target thickness of 3×10^{15} atoms/cm², is currently under data taking. Another unpolarized internal target was used at the VEPP-3 facility [4] in Novosibirsk for electron/positron cross section measurements in order to detect a possible two-photon exchange effect. It has a similar design to that used in previous experiments at VEPP-3 [5], where a target thickness of $\approx 10^{15}$ atoms/cm² was reached. In the proposed Dark Light experiment [6] at Jefferson Lab, an unpolarized hydrogen gas target aiming at attaining a $\approx 10^{19}$ atoms/cm² thickness has been designed. This list does not intend to be exhaustive but shows the wide range of applications, the versatility and the reliability of polarized/unpolarized internal gas flow targets in electron/positron scattering experiments. All these targets use important differential pumping systems in order to remove the residual gas for maintaining the beam line vacuum pressure outside the target chamber. The novelty of our proposed target does not lie in the principle but rather in the high density that it will be able to reach. In the next sections we give a complete description of the whole system.

Table 1: Summary of gas flow targets used in various laboratories including the proposed ones at JLab.

	Gas	Length (cm)	Thickness (atoms/cm ²)	Temperature (K)	Polarized
HERMES	^3He	40	6×10^{15}	15	yes
BLAST	H_2/D_2	60	7×10^{13}	100	yes
OLYMPUS	H_2	27	3×10^{15}	25	no
VEPP-3	H_2	40	$\approx 10^{15}$	-	no
Dark Light	H_2	25	$\approx 10^{19}$	25	no
This proposal	H_2	4	$\approx 10^{18}$	25	no

In this experiment we propose to use a windowless cryo-cooled hydrogen gas flow target of thickness $t \sim 1 \times 10^{18}$ hydrogen atoms/cm² at a beam current of 10 nA. The choice of such a target is driven by several experimental considerations. Since we propose to make the measurements at very low Q^2 , the scattered electrons in ep elastic scatterings will be detected at very forward angles (as low as $\sim 0.5^\circ$) and thus very close to the beam line. As a consequence, in order to minimize the overall background in the experiment, a windowless target-cell design is the best option. Indeed, in the recent precision measurements of elastic ep scattering cross sections from MAMI at Mainz [7], the primary source of background was the elastic and quasielastic scattering off the nuclei in the walls of the closed-cell target. Furthermore, to reach such a high target density while keeping a manageable mass flow rate, the cooling of the hydrogen gas becomes mandatory.

The windowless cryo-cooled hydrogen gas flow target consists of a T-shaped cylindrical cell with an inlet and two outlets pressurized to a pressure p_1 at a temperature T_1 by a constant inlet feed. Figure 1 shows the principles of the windowless target: the gas flows out into the beam pipe vacuum through the open-ended target cell, *i.e.*, two small conductance tubes (outlets) of half-length $L/2$ and diameter D concentric to the beam axis upstream and downstream of the cell. The density profile along the target length which is approximately triangular in shape is also shown in Fig. 1. In order to reduce a potential misalignment of the target cell induced by the vacuum in the target chamber and for a better position stability, three 25 μm diameter Tungsten wires oriented at 120° from each other are connected to each of the outlets of the cell (see the top right picture in Fig. 4).

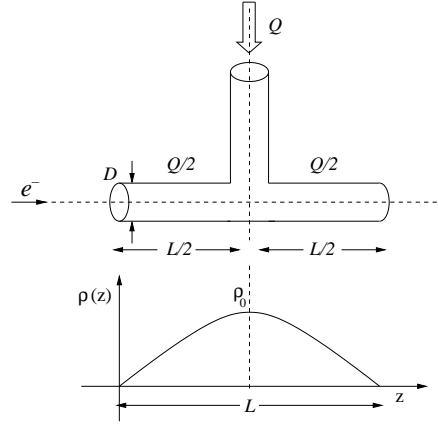


Figure 1: Schematic showing the principles of the windowless gas flow target (top) and the triangular density profile along the target length (bottom).

The mass flow rate, Q , of a gas through an outflow tube expressed in terms of volume flow normalized to a temperature T_0 times the gas pressure is:

$$Q = \frac{\pi}{4} D \text{Re} \mu R \frac{T_0}{M}, \quad (1)$$

where R is the universal gas constant, Re is the Reynolds number, μ is the dynamic viscosity of the gas. Thus, for a given Q and μ , the Reynolds number and Mach number η_1 can be determined from which, for a given cell temperature T_1 , the cell pressure p_1 can be calculated. The resulting target thickness $t = \rho L$, where ρ is the particle density and L is the target length, is

$$\begin{aligned} t &= \frac{N_A}{V_{\text{mol}}} L \frac{p_1}{736 \text{ Torr}} \frac{273 \text{ }^\circ\text{K}}{T_1} \\ &= 1.00 \times 10^{19} \frac{L}{\text{cm}} \frac{p_1}{\text{Torr}} \frac{^\circ\text{K}}{T_1}, \end{aligned} \quad (2)$$

where N_A is Avogadro constant and V_{mol} is the molar volume. The specific hydrogen target proposed for the proton charge radius experiment is a thin-walled (30 μm thick) Kapton tube with the following dimensions and parameters:

$$L = 4 \text{ cm}; \quad D = 4 \text{ mm}; \quad \rho_0 = 2.5 \times 10^{17} \text{ H}_2/\text{cm}^3 \quad (\text{initial density at target center.}) \quad (3)$$

With these parameters one finds

$$\eta_1 \approx 0.3; \quad \text{Re} \approx 207; \quad p_1 \approx 6.8 \text{ Torr (at } 273^\circ\text{K).} \quad (4)$$

The total particle flux through both ends of the target cell is $\varphi = \rho_0 C \approx 2.2 \times 10^{20} \text{ H}_2/\text{s}$ for a mass flow rate of $Q \approx 6.3 \text{ Torr-l/s}$ at $T_1 = 25^\circ\text{K}$. The gas flow remains laminar ($\text{Re} \leq 1200$) up to mass flow of $Q = 150 \text{ Torr-l/s}$. Over an average length of about 1.5 cm for a triangular shaped density profile along the target length, a mass flow rate of $Q \approx 6.3 \text{ Torr-l/s}$ can produce the required thickness of $10^{18} \text{ hydrogen atoms/cm}^2$.

3.1 Target cell

The target cell will consist of a 4 cm long, 8 mm diameter and $30 \mu\text{m}$ thick Kapton straw tube with two $10 \mu\text{m}$ thick Kapton end-caps having central holes of 4 mm diameter along the incident beam axis. A 6 mm inner-diameter $75 \mu\text{m}$ -thick Kapton vertical tube will be glued to the central hole in the horizontal Kapton straw tube forming a T-shaped target cell, as shown in Fig 2. The glue joints will be reinforced with thin wedge-shaped rings of Rohacell-31 for increased strength and stability. The free end of the vertical part of the T-shaped target cell will be attached to the outlet of the cryo-cooler using a compression type fitting. The cell will be anchored to the primary target vacuum chamber using $25 \mu\text{m}$ tungsten wires placed at 120° with each other around the tube. This cell design will ensure a more uniform distribution of the hydrogen gas compared to the triangular profile shown in Fig. 1. The larger diameter of the cell compared to the entrance and exit apertures will ensure reduced backgrounds from the beam halo at the cost of slightly reduced effective target thickness.

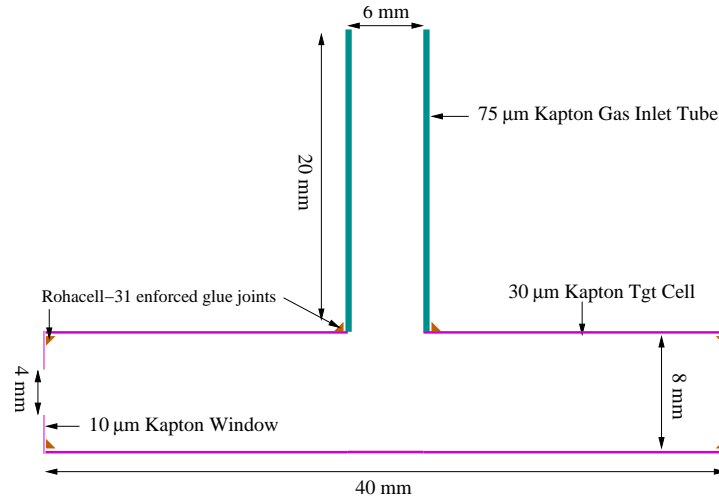


Figure 2: Schematic of the target cell design.

3.2 Target cooling system

The inlet hydrogen gas will be cooled by a custom SHI CP204 10K cryo-cooler from Janis Research Company. A copper tube will be wrapped around the two cooling stages of the refrigerator.

One end of this tube will connect at room temperature to the gas feed through and the other end will be connected to the target cell. Temperature sensors and heaters will be connected to each cooling stage and the temperature will be monitored by a LakeShore model 336 temperature controller. This setup will greatly simplify the design of the target cell by not requiring an independent cooling of the target cell itself.

3.3 Target pumping system

A mass flow rate of $Q \approx 6.3$ Torr-l/s has a major demand on the overall pumping capacity of the system in order to maintain the original vacuum pressure $p_0 \approx 5 \times 10^{-6}$ Torr of the beam line. This can be achieved by a two-stage differential pumping system. Conductance limits will be installed between stages in order to improve the overall pumping efficiency. In the first stage two Pfeiffer HiPace 3400 MC turbomolecular pumps with a pumping capacity of ≈ 2950 l/s for H_2 each will be directly connected to the target chamber in the transverse direction with respect to the beam. The second stage consists of one Pfeiffer HiPace 1500 turbomolecular pump with a pumping speed of ≈ 1150 l/s for H_2 upstream and downstream of the target connected to secondary chambers. All of these four pumps will be backed up with four Pfeiffer HiPace 60P turbomolecular pumps and four Varian TriScroll 300 roughing pumps. With the two large HiPace 3400 MC connected to the interaction chamber, one can reach a background pressure of $\approx 5 \times 10^{-3}$ Torr. With a diameter of 1.5 cm for the circular aperture in the baffles between the two pumping stages, the pressure in the second stage will be $\approx 6 \times 10^{-6}$ Torr. The pressure will be read out with two ion gauges in the target chamber and the second pumping stage upstream of the target. A schematic of the target and pumping system setup is shown in Fig. 3. The whole system without the backing pumps is shown in Fig. 4.

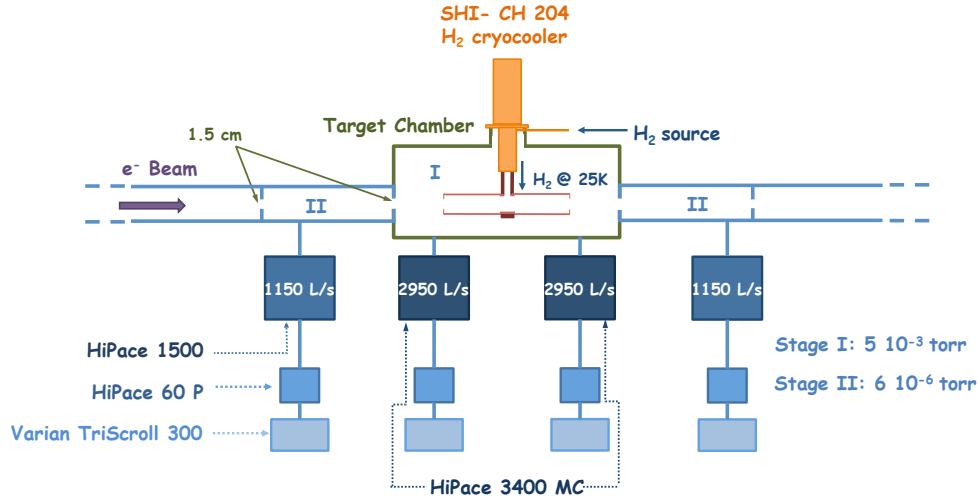


Figure 3: Schematic of the target and pumping system setup (not to scale).

The various technical parameters of the proposed target are summarized in Table 2.

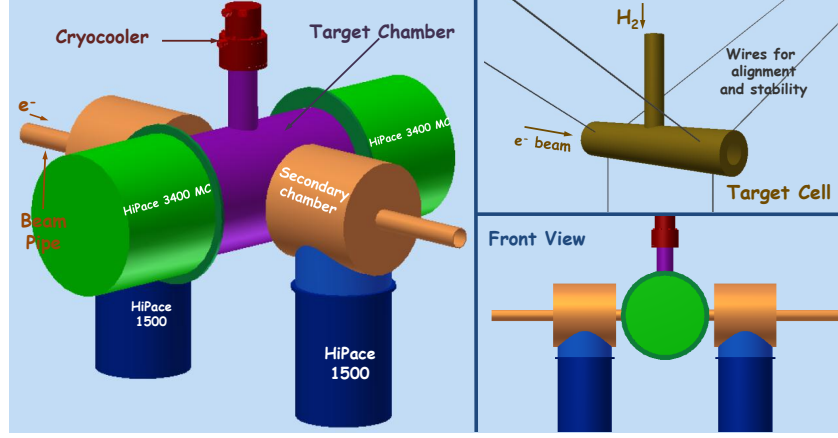


Figure 4: Global view of the target and pumping system installation.

Table 2: Parameters of the cryo-cooled windowless hydrogen gas flow target

Target length	4 cm
Target diameter	4 mm
Target cell material	Kapton 30 μm thick
Target temperature	25 K
Target thickness	1×10^{18} atoms/cm ²
Target central density	2.5×10^{17} H ₂ /cm ³
Gas mass-flow rate	6.3 Torr·l·s ⁻¹
Pressure: beamline	5×10^{-6} Torr
Pressure: target chamber	5×10^{-3} Torr
Pressure: 2 nd stage chamber	6.10^{-6} Torr

3.4 Target gas handling system

The gas handling system for the windowless hydrogen target is shown in Fig. 5. The beamline and target chamber parts of the vacuum system are discussed in Section 3.3. The remotely controllable gas handling system will allow the injection of hydrogen gas, at a known constant rate, into the cryo-cooler followed by the target cell. The hydrogen gas delivered from standard high-pressure gas cylinders will enter the gas manifold via a regulator and remotely controlled valve, the regulators will be set to approximately 0.5 bar. The hydrogen gas will be injected into the target cell via a mass flow-meter, operating at about 0.5 bar, and a thermovalve (temperature controlled needle valve).

The pressure at various points of the manifold including the entrance of the cryo-cooler and the target cell will be measured with total pressure baratron gauges. Other valves and lines shown in Fig. 5 will permit pumping the gas out of the manifold and the target cell via a small turbomolecular pump (30 l/s) system. All valves will be controlled by a programmable interlock system. The residual gas exiting from the target cell will not be recirculated back into the gas handling system

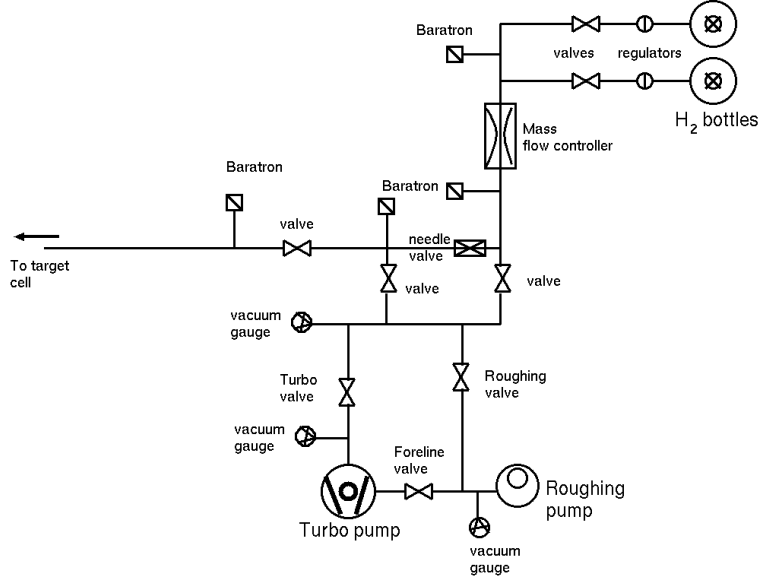


Figure 5: Schematic of the gas handling system.

but it will be vented out via dedicated exhaust lines installed in the experimental hall. The total volume of hydrogen gas that will be required for the entire running period of the experiment (15 days) is about 9.6 m^3 (equivalent to about two standard high-pressure gas cylinders).

3.5 Target vacuum chambers

The primary target vacuum chamber will be constructed from a custom 4-way Conflat flanged (CF) reducing cross with two 2-inch ports in the direction of the beam and two 16-inch ports transverse to the beam (horizontal). It will have two viewing ports inclined at 30° to the vertical and a gas inlet port on the top side. The bottom side of the chamber will have four height adjustable legs for support and alignment. The two secondary chambers will be constructed from custom 3-way CF crosses or cubes with two 2-inch ports and one 12-inch port.

3.6 Beamline integration of the target

The target vacuum chamber will be interfaced to the four vacuum pumps and the Hall-B beamline via CF flanged, edge-welded stainless steel bellows. The two bellows in the beam direction will have conductance limiting baffles made from Kapton foils with a 1.5 cm diameter circular aperture. The complete target system will be integrated into the Hall-B beamline via stainless steel bellows, these bellows will also have conductance limiting baffles made from Kapton foils with a 1.5 cm diameter circular aperture. The target chamber and vacuum pumps will be supported by beam-line girders and additional support stands, as shown in Fig. 6. The target vacuum chamber will be built with four adjustable legs for alignment. The height of these legs will be adjustable via custom built $100 \mu\text{m}$ pitch screws. Survey monuments will be mounted at appropriate locations to help align the system before and after pump down. Two vacuum view-ports with graduated cross-hairs are also included in the target vacuum chamber to monitor the target cell alignment. The complete

target system will have a footprint of $1.6 \times 1.4 \text{ m}^2$ and will easily fit in the 3 m^2 space available in the Hall-B beamline.

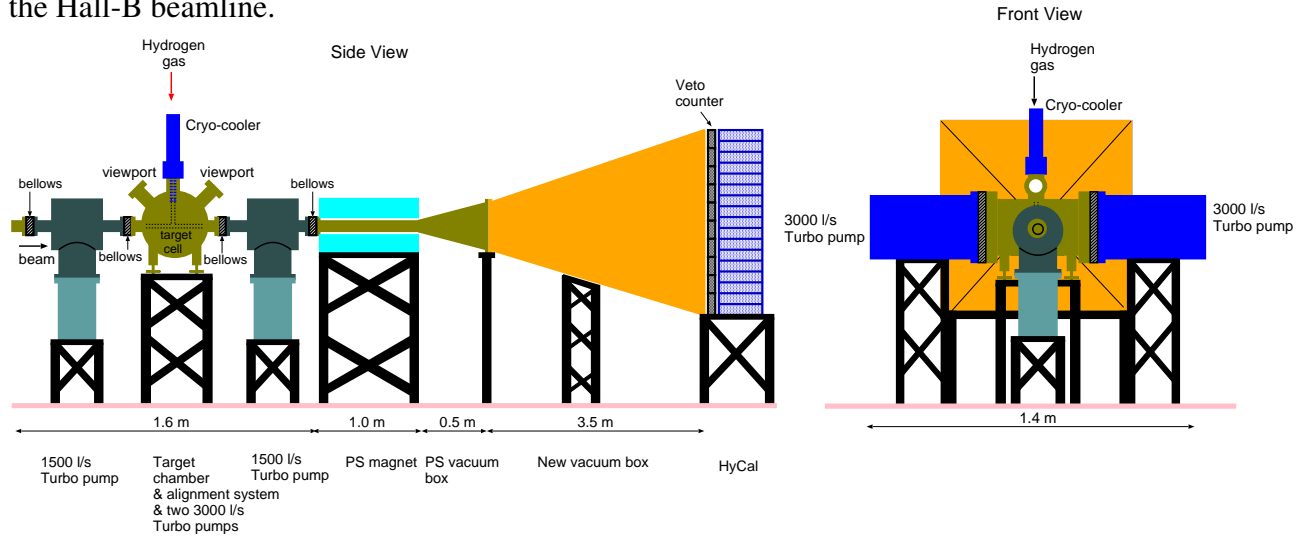


Figure 6: Schematic of the complete installation (along the beamline and front-view) of the target.

4 Beam halo studies in Hall-B

Recent measurements of the transverse beam profile in Hall B was performed with sufficient dynamic range to provide a mechanism for determining the acceptability of the delivered beam such that the ratio of beam signal to background from non-target interactions is at the level of $\sim 10^7$ level.

The beam profile was measured by correlating a wire scanner position with count rates in a pair of photomultiplier tubes (PMTs) located downstream of the wire scanner. To observe and measure the beam width with greater sensitivity for a large dynamic range the integrating CLAS wire scanner was used. The wire configuration and support frame for the integrating wire scanner are shown in Fig. 7. The wire configuration consists of 25 μm diameter X and Y wires, 1 mm diameter X and Y wires, and a 1 mm \times 10 mm X plate. All wires are made out of Fe and the plate is stainless steel. This wire scanner is 5 m upstream of the PMT pair.

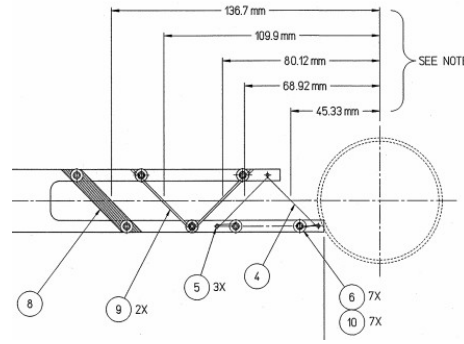


Figure 7: Mechanical schematic of the wire/plate support structure. The thin wire is 25 μm in diameter. The thick wire is 1 mm in diameter. The plate is 1 mm \times 10 mm. The wire frame is moved into the beam along a 45° axis with respect to the horizontal axis.

Beam profile scans were performed with a 5.5 GeV electron beam during the current running experiment in Hall-B. The electron beam was specially well tuned to do studies of the beam halo for the proton charge radius measurement. Several scan were taken with different beam intensities and motor speeds for the wire scanner.

The 25 μm wires are used to scan the X and Y core profiles of the beam while the 1 mm wires are used to scan the halo parts on either side of the beam's core (the PMTs get saturated with the high count rates from the thick 1 mm wires in the peak regions). Figures 8 and 9 show the X and Y beam profiles obtained with a beam intensity of 1 nA and a motor speed of 0.07 mm/s.

Offline analysis was performed on the raw data in order to combine the 25 μm wire data with the 1 mm wire. The technique used is the same as given in [8]. The beam size (< 0.1 mm) is small compared to the 1 mm wire diameter. Therefore, this data must be differentiated before they can be combined with the 25 μm wire data with an appropriate scale factor.

Figure 10 shows the peak signal from the 25 μm wire data scaled by 2000 and the differentiated data from the 1 mm wire.

Preliminary results from the recent beam profile measurements shown in Fig. 10 look promising for this proposed experiment and further analysis is ongoing.

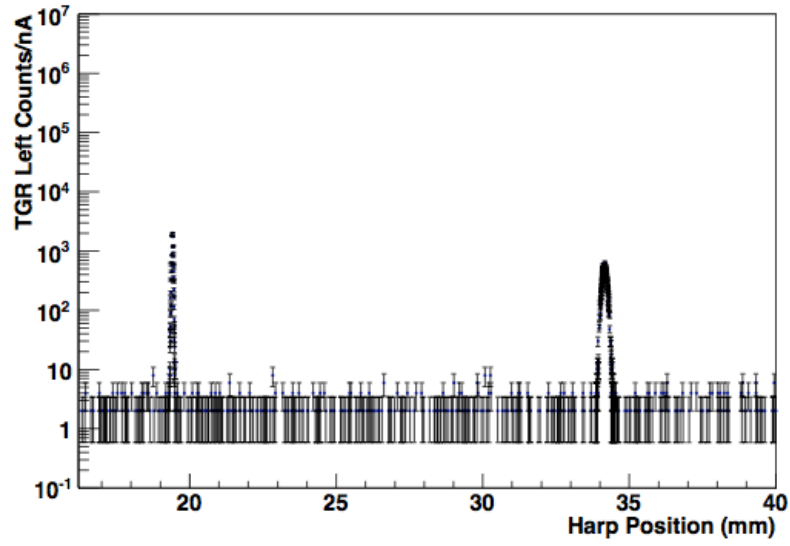


Figure 8: The X (left peak) and Y (right peak) beam profiles for a 1 nA beam intensity obtained by scanning the $25\ \mu\text{m}$ wires across the beam.

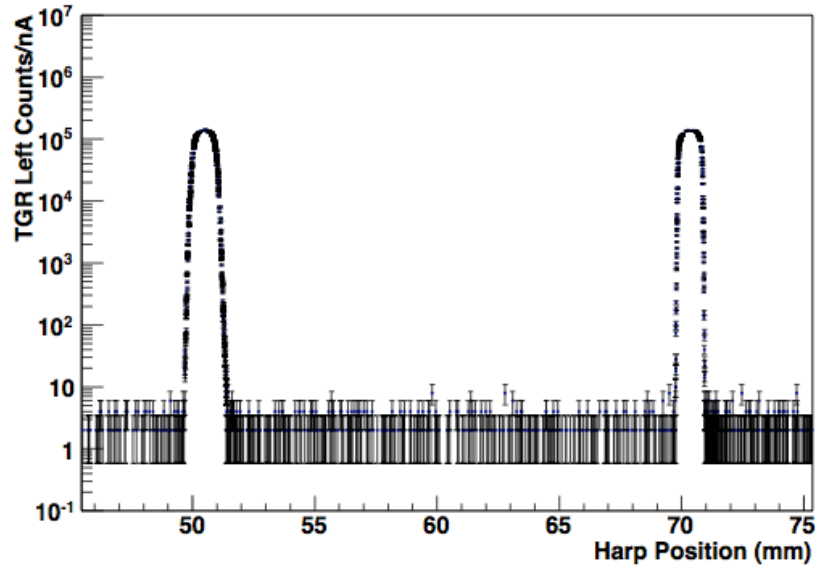


Figure 9: The X (left peak) and Y (right peak) beam profiles for a 1 nA beam intensity obtained by scanning the 1 mm wires across the beam.

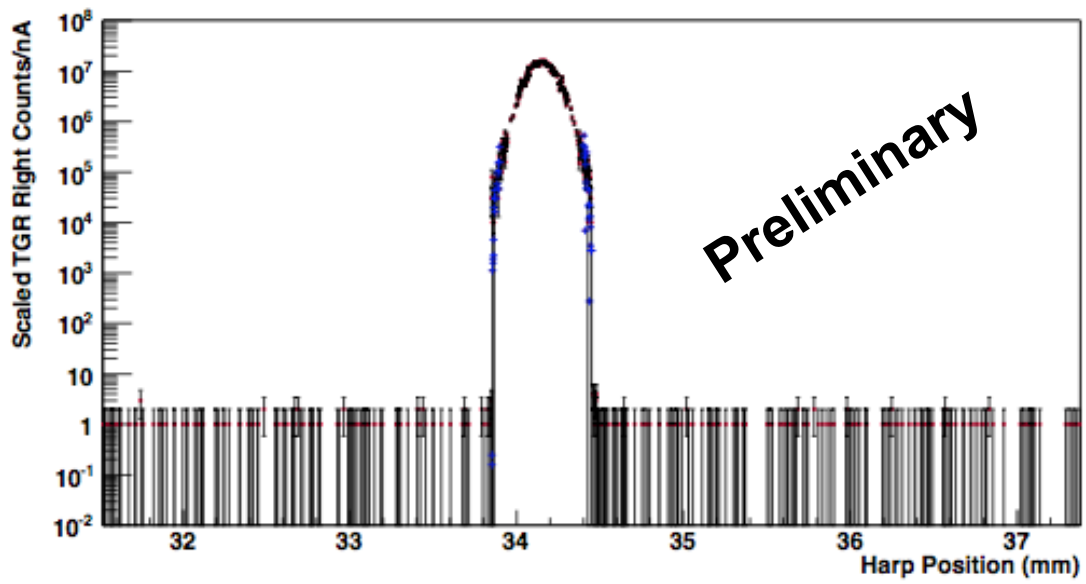


Figure 10: The X beam profile combining the 25 μm (red points) and the 1 mm (blue points) wire data. The count rate is normalized to the incident beam current.

5 Radiative corrections extended to Q^2 of 10^{-4} GeV²

5.1 Radiative corrections to ep elastic scattering beyond the URA

As stated in the original proposal [9] we used the codes MASCARAD [10] to calculate the radiative corrections and ELRADGEN [11] to generate radiative events for the full Monte Carlo simulation of the experiment. Both codes use the ultra relativistic approximation (URA) $m_e \ll Q^2$. We performed a new calculation of these corrections beyond the URA following the formalism developed in [12] and updated both codes accordingly. Different contributions to the cross section were recalculated by including the electron mass where it has been neglected. The ep elastic cross section is given by:

$$\sigma = \sigma_0(1 + \delta_{VR} + \delta_{vac} - \delta_{inf})e^{\delta_{inf}} + \sigma_F, \quad (5)$$

with σ_0 being the Born cross section, δ_{VR} and δ_{vac} the corrections coming from soft photon radiation and effect of vacuum polarization, respectively. The term δ_{inf} accounts for multi-photon emission when $Q^2 \rightarrow 0$. It can be chosen arbitrarily and was set to the same expression as in the original code. Details about this exponentiation procedure can be found in [13]. σ_F is the infrared free correction from the hard photon emission (bremsstrahlung). Expressions for the different corrections are given in Appendix A.

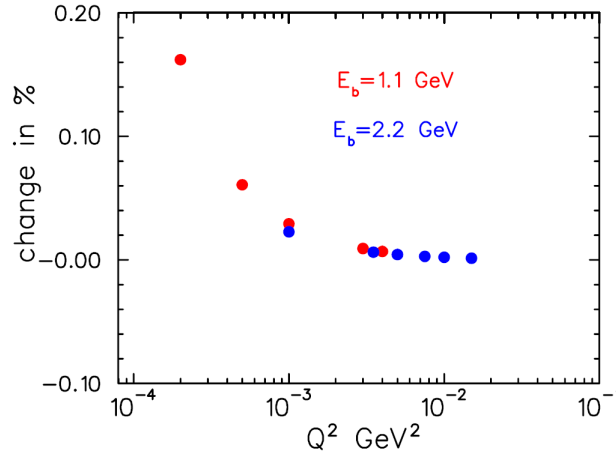


Figure 11: The percent change between the cross section calculated beyond the URA and that in the URA.

Figure 11 shows the change in percent between the cross section σ using the URA and that obtained beyond the URA. It is seen that the change is at most 0.2% for the lowest Q^2 value of our proposed kinematics and of course decreases when Q^2 value increases due to the leading order term $\ln\left(\frac{Q^2}{m^2}\right)$. This also shows the good accuracy of the URA. It is important to point out that the approximation no longer holds well for $Q^2 \approx 10^{-5}$ GeV² since the change reaches few percents. Figure 12 shows the ep radiative corrections for $E_{\text{beam}}=1.1$ GeV (bottom panel) and $E_{\text{beam}}=2.2$ GeV (top panel) as a function of the inelasticity $v = 2M(E - E') - Q^2$ (missing mass) for

different values of Q^2 . The red box in the figure shows the range of v spanned by the kinematic settings in the experiment.

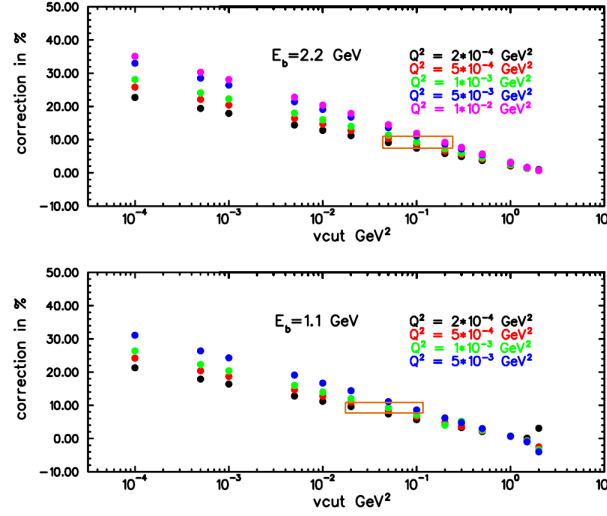


Figure 12: ep radiative corrections at 1.1 GeV (bottom panel) and at 2.2 GeV (top panel) as a function of the inelasticity v .

Figure 13 shows the ep radiative corrections over the full kinematical range of both beam energy settings obtained using the modified code. Values of $v = 0.04 \text{ GeV}^2$ and 0.1 GeV^2 , corresponding to the central value of the v range in Fig. 12, are for $E_{\text{beam}}=1.1 \text{ GeV}$ and $E_{\text{beam}}=2.2 \text{ GeV}$, respectively. These values will need to be determined experimentally. However, we see that the radiative corrections depend only weakly (few percent level) on this value in the ranges of interest. A correction of $9\% \leq \delta \leq 12\%$ at $E_{\text{beam}}=1.1 \text{ GeV}$ was found and at $E_{\text{beam}}=2.2 \text{ GeV}$, $10\% \leq \delta \leq 13\%$.

5.2 Radiative corrections to Møller scattering

The Møller radiative corrections (events) were calculated (generated) using the most advanced codes MERA [14] and MERADGEN [15]. These programs have been well tested [16] and they give stable results up to $Q^2 \approx 10^{-7} \text{ GeV}^2$. Figure 14 shows the Møller radiative corrections as a function of Q^2 for both incident beam energies. Corrections between 1% and 3% were found for both energies.

The effect of radiative corrections on the scattered electron energy vs angle for ep elastic and Møller scattering events are shown in Fig. 15, where elastic and Møller events with and without radiative corrections were simulated for $E_{\text{beam}} = 1.1 \text{ GeV}$.

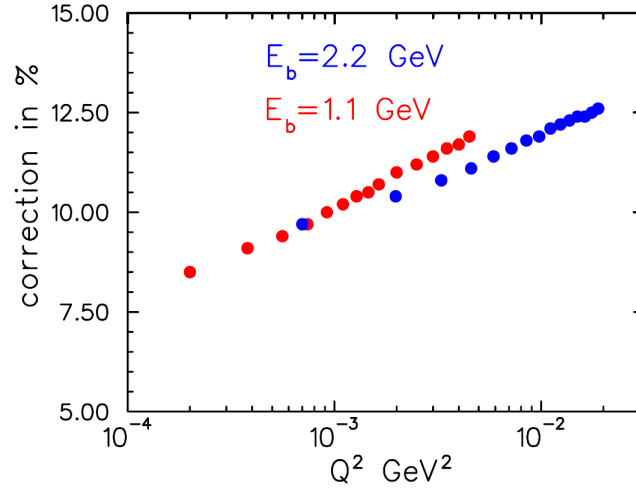


Figure 13: ep radiative corrections at 1.1 GeV ($2 \cdot 10^{-4} \leq Q^2 \leq 5 \cdot 10^{-3}$ GeV²) and at 2.2 GeV ($7 \cdot 10^{-4} \leq Q^2 \leq 2 \cdot 10^{-2}$ GeV²).

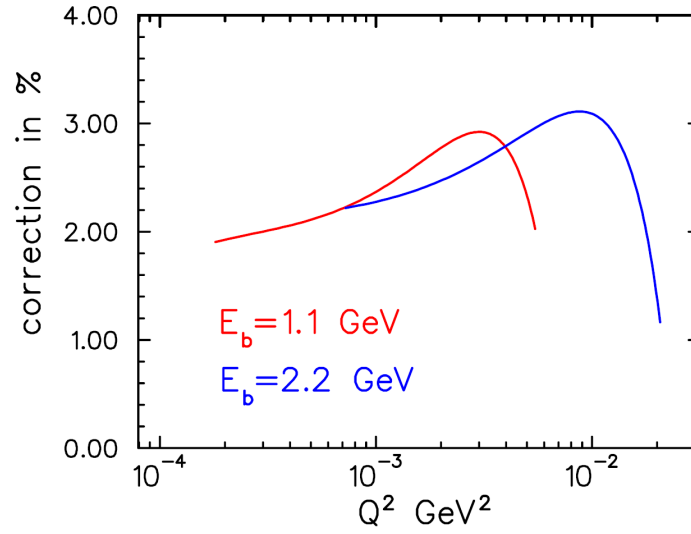


Figure 14: Møller radiative corrections at 1.1 GeV and at 2.2 GeV.

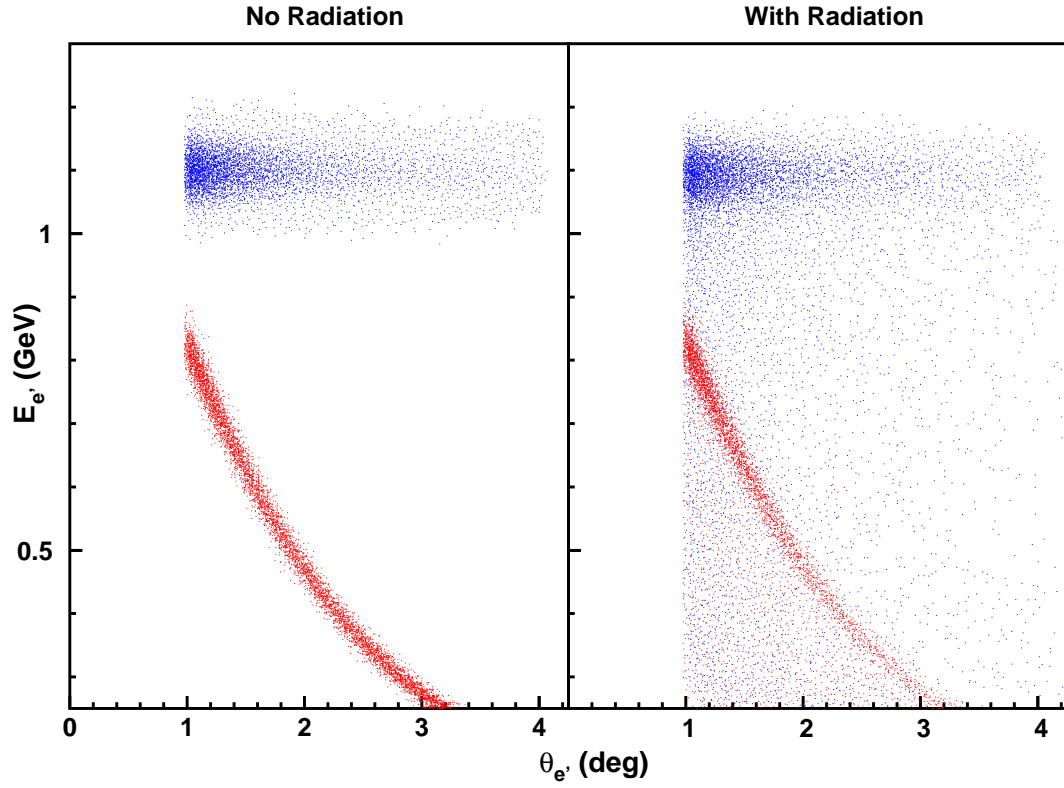


Figure 15: The distribution of scattered energy (E_e') vs angle (θ_e) for ep elastic (blue) and Møller events (red) simulated with and without radiative corrections are shown for $\theta_e > 1.0^\circ$. These distributions are for $E_{beam} = 1.1$ GeV.

6 Monte Carlo simulation of the experimental background

In order to study the interaction between the beam halo and the target, a Monte Carlo simulation code based on GEANT was developed.

6.1 Geometry

The full geometry in the simulation includes the hydrogen gas flow target, the target cell and the PbWO_4 calorimeter.

- i. The gas flow target was built by 10 slices of hydrogen gas with different densities which linearly decreases from the center to the edge. The average thickness at the center of the hydrogen target is 1.0×10^{18} H atoms/cm².
- ii. The simulated target cell geometry is identical to the one described in Section 3.1 including the 20 mm long 75 μm thick Kapton gas inlet tube. The chemical formula for Kapton was implemented into GEANT. The simulated PbWO_4 calorimeter consists of 34×34 modules of dimensions $2.05 \times 2.05 \times 18.0$ cm³.

6.2 Physics processes

A standard GEANT electromagnetic event generator was used in the simulation code. It consists of electromagnetic processes for photons, electrons, protons, pions, muons and other generic ions. The electron-proton elastic, Møller scattering and bremsstrahlung process are included in this event generator. In order to obtain a precise simulation result of the electron transport in a very low density hydrogen gas, the GEANT multiple scattering process model was replaced by a single scattering process model in this event generator [17]. Furthermore, some GEANT physics models of nuclear reactions, such as electron-nuclear reaction, positron-nuclear reaction and photon-nuclear reaction, were also implemented in the simulation.

6.3 Event generator for beam halo

In this experiment, the most important source of background is the beam halo target interaction. The electron beam was simulated using a normal distribution with a $\sigma = 80 \mu\text{m}$, and the beam halo was generated following a uniform distribution of width ± 20 mm. The beam signal (peak) to noise (beam halo) ratio was taken to be 10^7 which is similar to the result of the beam studies described in section Section 4. Table 3 summarizes the target and beam parameters used in the Monte Carlo simulation.

Table 3: Target and beam parameters for Monte Carlo simulation

Target thickness	1×10^{18} atoms/cm ²
Beam intensity	$I_e = 10$ nA
Beam signal width	$\sigma = 80 \mu\text{m}$
Beam signal/halo ratio	10^7
Beam halo (flat) width	± 20 mm

6.4 Simulation results

ep elastic events and background from the Kapton target cell and gas-inlet tube were generated in the angular range $0.8^\circ < \theta_e < 3.8^\circ$. Figures 16 and 17 show the energy E' of the scattered electron versus the scattering angle θ_e at $E_0 = 1.1$ GeV and 2.2 GeV, respectively.

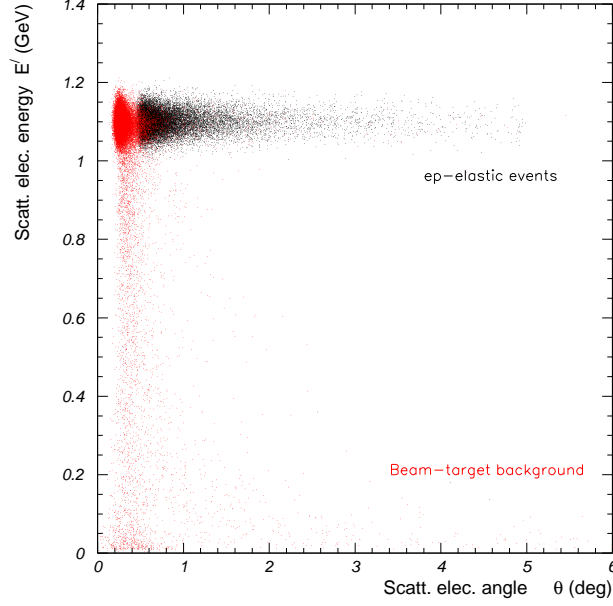


Figure 16: The energy *vs.* scattering angle distribution of ep elastic scattered electrons and background from the target cell and gas-inlet tube at $E_0 = 1.1$ GeV.

The event selection criteria for comparing ep elastic to background events were:

- (a) (scattered electron energy) $> 0.3 \times$ (Beam energy);
- (b) charged particles only (no photons);
- (c) particles in angular range $0.8^\circ < \theta_e < 3.8^\circ$.

Figures 18 and 19 show the angular distributions of the ep elastic and the background events binned in 0.3° bins at $E_0 = 1.1$ GeV and 2.2 GeV, respectively.

The ratio of background to ep elastic scattered electrons at the higher incident beam energy setting at $E_0 = 2.2$ GeV varies between 0.7% at $\theta_e = 1.0^\circ$ to 1.9% at $\theta_e = 3.6^\circ$. The same ratio at $E_0 = 1.1$ GeV is smaller by a factor ~ 2 . The average ratio of background to ep elastic is $\sim 1.2\%$ at $E_0 = 2.2$ GeV and $\sim 0.5\%$ at $E_0 = 1.1$ GeV. More comprehensive GEANT simulations are ongoing.

It is projected that with empty target running at regular intervals during the experiment, one can safely account for the effects of any beam instability and contributions from the beam halo to reach the proposed precision of 0.6% for the measurement of $\langle r_p \rangle$.

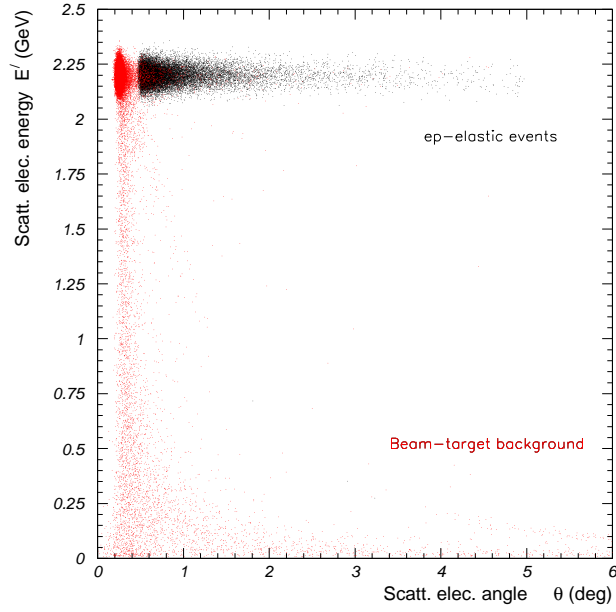


Figure 17: The energy *vs.* scattering angle distribution of *ep* elastic scattered electrons and background from the target cell and gas-inlet tube at $E_0 = 2.2$ GeV.

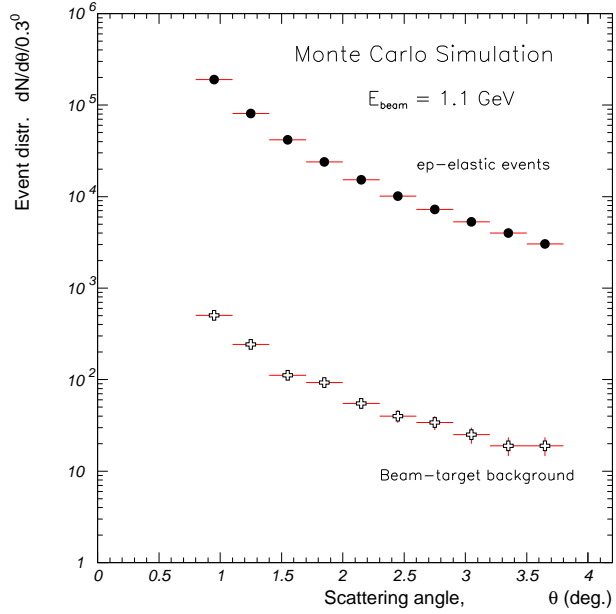


Figure 18: The angular distribution of *ep* elastic scattered electrons and background from the target cell and gas-inlet tube at $E_0 = 1.1$ GeV.

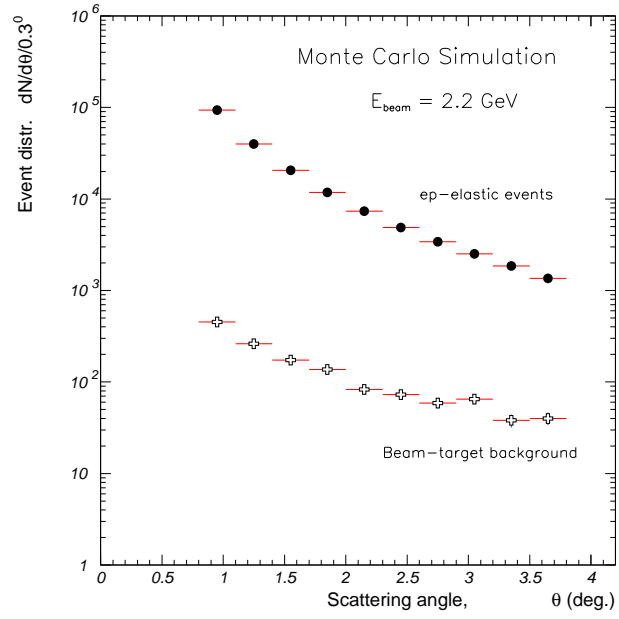


Figure 19: The angular distribution of ep elastic scattered electrons and background from the target cell and gas-inlet tube at $E_0 = 2.2 \text{ GeV}$.

7 Simulation of the effect of radiative corrections on the extraction of $\langle r_p \rangle$

An event generator for ep elastic scattering was used to study the effect of radiation on the extraction of the charge radius from the simulated events. In the event generator we used the parametrization $G_E = 1 - \frac{Q^2}{6} \langle r_p^2 \rangle$ in calculating the ep cross section. The radiative correction code described in Sec. 5 was incorporated into the event generator. Just the geometrical acceptance was used as the detector acceptance and Gaussian smearing was used to simulate the effect of detector resolution. Events were generated for electron beam energy of 1.1 and 2.2 GeV both with and without radiative corrections. The cross section and then G_E as a function of Q^2 was extracted from the simulated data. The resulting G_E as a function of Q^2 was fitted to a straight line, and the slope of the line gives us the value of $\langle r_p \rangle$. The results for events simulated with and without radiation are shown in Fig. 20. The values of $\langle r_p \rangle$ used in the simulation is compared to the values extracted by analyzing the simulated data and the effect of the radiative corrections was found to be very small.

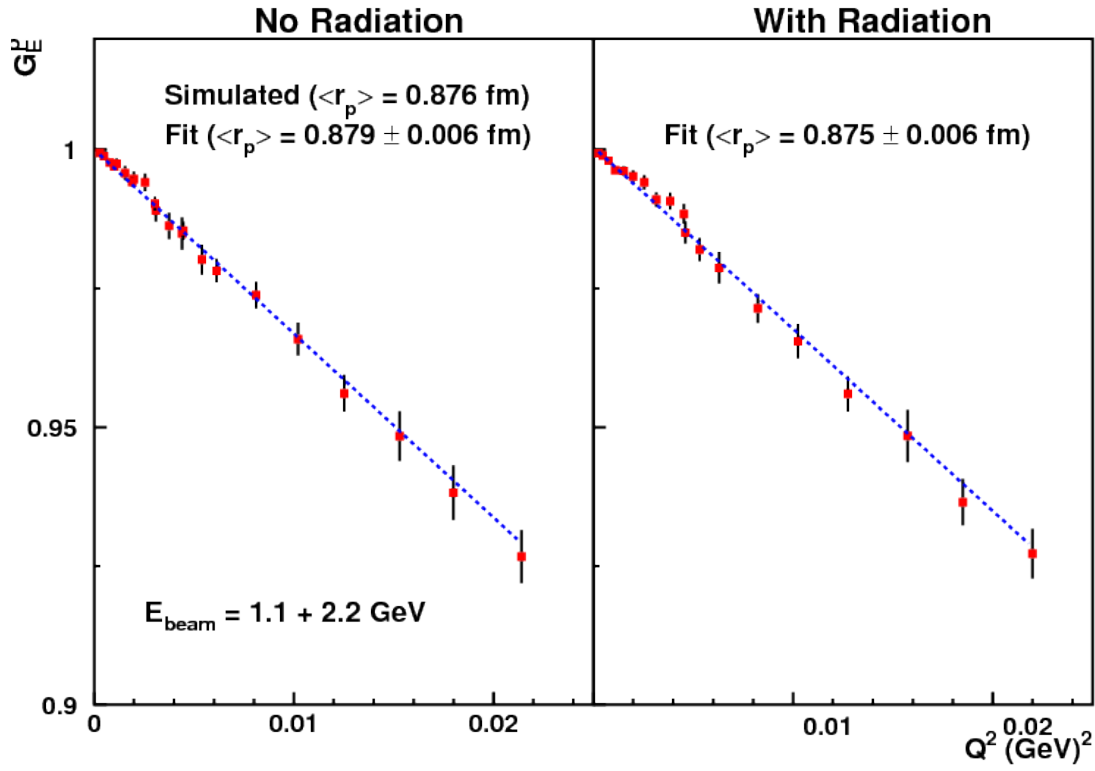


Figure 20: The extracted $\langle r_p \rangle$ from simulated events with and without radiative corrections.

8 Summary

The physics motivation of the proton charge radius remains very strong and urgent. Our proposed experiment at Jefferson Lab will address this important and fundamental physics quantity in a timely and unique way. We believe we have addressed all the technical issues raised by the PAC38 reports and we are confident to achieve the proposed accuracy. We have submitted to NSF a MRI proposal to build the target for this experiment and the collaboration will be ready for this experiment within a year that funds are in place for the construction of this target. This experiment, with the requested 15 days of beam time, will have a direct impact on the “*proton charge radius crisis*” currently developing in hadronic physics.

References

- [1] D. DeSchepper *et al.*, Nucl. Instr. and Meth. A **419**, 16 (1998).
- [2] D. Cheever *et al.*, Nucl. Instr. and Meth. A **556**, 410 (2006).
- [3] D. Hasell *et al.*, “A proposal to definitively determine the contribution of multiple photon exchange in elastic lepton-nucleon scattering”, 2008
(<http://web.mit.edu/OLYMPUS/DOCUMENTS/Proposal-PRC-20080909.pdf>).
- [4] A.V. Gramolin *et al.*, Nucl. Phys. B **219** 1, (2011).
- [5] M.V. Dyug *et al.*, Nucl. Instr. and Meth. A **495**, 8 (2002).
- [6] P. Fisher *et al.*, “A proposal for the Dark Light Experiment at the Jefferson Laboratory Free Electron Laser”, 2010 ([http://wwwold.jlab.org/exp_prog/PACpage/PAC37/proposals/Proposals/New Proposals/PR-11-008.pdf](http://wwwold.jlab.org/exp_prog/PACpage/PAC37/proposals/Proposals/New%20Proposals/PR-11-008.pdf)).
- [7] J.C. Bernauer *et al.*, Phys. Rev. Lett. **105**, 242001 (2010).
- [8] A.P. Freyberger, “Large Dynamic Range Beam Profile Measurements”, DIPAC 2005, June 6-8, 2005, Lyon, France.
- [9] A. Garparian *et al.*, “High Precision Measurement of the Proton Charge Radius”, 2011
(http://www.jlab.org/exp_prog/proposals/11/PR12-11-106.pdf).
- [10] A. Afanasev, I. Akushevich, N. Merenkov, Phys. Rev. D **64**, 113009 (2001).
- [11] I. Akushevich, O.F. Filoti, A. Ilyichev, N. Shumeiko, arXiv:1104.0039v1 [hep-ph], 2011.
- [12] D. Bardin, N. Shumeiko, Nucl. Phys. B **127**, 242 (1977).
- [13] N. Shumeiko, Yad. Fiz. **29**, 1571 (1979).
- [14] A. Ilyichev, V. Zykunov, Phys. Rev. D **72**, 033018 (2005).
- [15] A. Afanasev, E. Chudakov, A. Ilyichev, V. Zykunov, Comput. Phys. Commun. **176**, 218 (2007).
- [16] A. Ilyichev, National Center of Particle and High Energy Physics, Minsk, Belarus (private communication).
- [17] V.N. Ivanchenko, O. Kadri, M. Maire, L. Urban, Journal of Physics: Conference Series **219**, 032045 (2010).

Appendices

A Expressions for radiative corrections beyond the URA

The total cross section for ep elastic scattering is given by the expression:

$$\frac{d\sigma}{dQ^2} = \frac{d\sigma_0}{dQ^2} (1 + \delta_{VR} + \delta_{vac} - \delta_{inf}) e^{\delta_{inf}} + \sigma_F, \quad (6)$$

with the various terms as:

The Born cross section:

$$\frac{d\sigma_0}{dQ^2} = \frac{2\pi\alpha^2}{S^2} \sum_i \theta_B^i \mathcal{F}_i. \quad (7)$$

The infrared-free sum of factorized part of soft photon emission and vertex correction:

$$\begin{aligned} \delta_{VR} = & \frac{\alpha}{\pi} \left(2 \left((Q^2 + 2m^2) L_m - 1 \right) \ln \left(\frac{v_{max}}{mM} \right) + \frac{1}{2} (SL_S + (S - Q^2) L_X^0) + S_\phi \right. \\ & \left. + \left(\frac{3}{2} Q^2 + 4m^2 \right) L_m - 2 - \frac{Q^2 + 2m^2}{\sqrt{\lambda_m}} \left(\frac{1}{2} \lambda_m L_m^2 + 2\Phi \left(\frac{2\sqrt{\lambda_m}}{Q^2 + \sqrt{\lambda_m}} \right) - \frac{\pi^2}{4} \right) \right) \end{aligned} \quad (8)$$

with Φ being the dilogarithm (Spence) function.

The vacuum polarization contribution:

$$\delta_{vac} = \sum_{i=e,\mu,\tau} \frac{\alpha}{\pi} \left[\frac{2}{3} (Q^2 + 2m_i^2) L_m^i - \frac{10}{9} + \frac{8m_i^2}{3Q^2} (1 - 2m_i^2 L_m^i) \right] \quad (9)$$

Soft photon radiation contribution:

$$\delta_{inf} = \frac{\alpha}{\pi} \left(\ln \frac{Q^2}{m^2} - 1 \right) \ln \left(\frac{v_{max}^2}{S(S - Q^2)} \right) \quad (10)$$

The infrared-free cross section of the bremsstrahlung process:

$$\sigma_F = -\frac{\alpha^3}{2S^2} \int_0^{v_{max}} dv \int_{\tau_{min}}^{\tau_{max}} \frac{d\tau}{1 + \tau} \int_0^{2\pi} d\phi \sum_{i,j} \left(R^{j-2} \theta_{ij} \frac{\mathcal{F}_i}{Q^4} - 4F_{IR} \theta_i^B \frac{\mathcal{F}_i^0}{\left(1 + \frac{R\tau}{Q^2}\right)^2} \right) \quad (11)$$

where:

$$\begin{aligned}
S &= 2EM \\
X &= 2E'M \\
L_m &= \frac{1}{\sqrt{\lambda_m}} \ln \frac{\sqrt{\lambda_m} + Q^2}{\sqrt{\lambda_m} - Q^2} \\
\lambda_m &= Q^2(Q^2 + 4m^2Q^2) \\
L_S &= \frac{1}{\sqrt{\lambda_S}} \ln \frac{S + \sqrt{\lambda_S}}{S - \sqrt{\lambda_S}} \\
L_X^0 &= \frac{1}{\sqrt{\lambda_X^0}} \ln \frac{S - Q^2 + \sqrt{\lambda_X^0}}{S - Q^2 - \sqrt{\lambda_X^0}} \\
\lambda_X^0 &= (S - Q^2)^2 - 4m^2M^2
\end{aligned}$$

The θ functions in σ_F are given by:

$$\begin{aligned}
\theta_B^1 &= Q^2 - 2m^2 \\
\theta_B^2 &= \frac{1}{2M^2} [S(S - Q^2) - M^2Q^2] \\
\theta_{11} &= 4(Q^2 - 2m^2)F_{IR} \\
\theta_{12} &= 4\tau F_{IR} \\
\theta_{13} &= -4F - 2\tau^2 F_d \\
\theta_{21} &= \frac{2}{M^2}(SX - M^2Q^2)F_{IR} \\
\theta_{22} &= \frac{1}{2M^2}(2m^2(S + X)F_{2-} + (S^2 - X^2)F_{1+} + 2(S - X - 2M^2\tau)F_{IR} - \tau(S + X)^2F_d) \\
\theta_{23} &= \frac{1}{2M^2}(4M^2F + (4m^2 + 2M^2\tau^2 - (S - X)\tau)F_d - (S + X)F_{1+})
\end{aligned}$$

$$\begin{aligned}
F_d &= \frac{F}{u_0 w_0}, \quad F_{1+} = \frac{F}{w_0} + \frac{F}{u_0} \\
F_{2\pm} &= Fm^2 \left(\frac{1}{u_0} + \frac{1}{u_0} \right), \quad F = 1/(2\pi\sqrt{\lambda_Q}) \\
\lambda_Q &= (Q^2 + v)^2 + 4M^2Q^2
\end{aligned}$$

The propagators are given by:

$$\begin{aligned}
w_0 &= \frac{1}{\lambda_Q} \left[Q^2(S + X) + \tau(S(S - X) + 2M^2Q^2) - 2M\sqrt{\lambda_z} \cos \phi_k \right] \\
u_0 &= \frac{1}{\lambda_Q} \left[Q^2(S + X) + \tau(S(S - X) - 2M^2Q^2) - 2M\sqrt{\lambda_z} \cos \phi_k \right]
\end{aligned}$$

with: $\lambda_z = (\tau - \tau_{min})(\tau_{max} - \tau)(SXQ^2 - M^2Q^4 - m^2\lambda_Q)$

B Original proposal PR12-11-106 for PAC38, August 22, 2011

(A New Proposal to Jefferson Lab PAC-38)

High Precision Measurement of the Proton Charge Radius

A. Gasparian (spokesperson and contact person), R. Pedroni
North Carolina A&T State University, Greensboro, NC 27411

M. Khandaker (co-spokesperson), V. Punjabi, C. Salgado
Norfolk State University, Norfolk, VA 23504

I. Akushevich, H. Gao (co-spokesperson), M. Huang,
G. Laskaris, S. Malace, M. Mezziane, C. Peng, Q.J. Ye, Y. Zhang, W. Zheng
Duke University, Durham, NC 27708

A. Deur, E. Pasyuk, S. Stepanyan, V. Kubarovsky,
D. Gaskell, M. Jones, D. Lawrence, S. Taylor, B. Wojtsekhowski, B. Zihlmann
Thomas Jefferson National Accelerator Facility, Newport News, VA 23606

J. Dunne, D. Dutta (co-spokesperson)
Mississippi State University, Mississippi State, MS 39762

L. Gan
University of North Carolina Wilmington, Wilmington, NC 28403

G. Gavalian
Old Dominion University, Norfolk, VA 23529

C. Crawford
University of Kentucky, Lexington, KY 40506

August 22, 2011

Abstract

We propose to perform a high precision $e - p$ elastic cross sections measurement at very low four-momentum transfer squared, Q^2 , from 10^{-4} to 10^{-2} $(\text{GeV}/c)^2$ range using a high resolution calorimeter. The absolute value of the $e - p$ cross sections will be controlled by a well known QED process, the Møller scattering, which will be continuously measured in this experiment within similar kinematics and the same experimental acceptances. The high precision differential cross sections, measured for the first time in this low Q^2 range, will allow a sub-percent and essentially model independent extraction of the proton charge radius. With that, this experiment will have a direct impact on the “*proton charge radius crisis*” currently developing in hadronic and atomic physics. We propose to perform this experiment in Hall B at Jefferson Lab using the unique low-intensity electron beam control capabilities of the hall and part of the PrimEx-II infrastructure.

Contents

1	Introduction	1
2	Electric and magnetic form factors of the nucleon and radii	1
3	Physics motivation	4
3.1	Proton charge radius from unpolarized $e - p$ elastic scattering	4
3.2	Double-polarization $e - p$ elastic scattering and proton charge radius	7
3.3	Proton charge radius from atomic measurements	8
3.4	Summary	9
4	Proposed experiment	10
4.1	Major advantages of the proposed experiment	10
4.2	Møller event selection methods	12
4.2.1	Single-arm Møller event selection method	12
4.2.2	Coincident event selection method	13
4.2.3	Integrated Møller cross section method	15
4.3	Relation to other experiments	15
5	Experimental apparatus	16
5.1	Introduction	16
5.2	Electron beam	16
5.3	Windowless gas flow target	17
5.4	High resolution forward calorimeter	19
5.4.1	Energy resolution	20
5.4.2	Position resolution	20
5.5	Veto counters	21
5.6	Electronics, data acquisition, and trigger	22
6	Experimental resolutions	24
6.1	Kinematics	24
6.1.1	$e - p$ scattering	24
6.1.2	Møller scattering	26
6.2	Resolutions	27
6.2.1	$e - p$ scattering	29
6.2.2	Møller scattering	29
7	Radiative corrections at forward angles	33
8	Extraction of proton charge radius	35
9	Statistics, event rate and beam time	38
10	Estimated uncertainties	40

11 Summary	42
References	43

1 Introduction

The strong interaction, which is responsible for the nucleon-nucleon interaction (nuclear forces), is one of the four fundamental forces in nature. Quantum chromodynamics (QCD), a theory with quarks and gluons as the underlying degrees of freedom is the accepted theory of strong interaction. QCD has two important features: asymptotic freedom and confinement. While the former refers to the feature that the strong coupling constant becomes weaker and weaker as energies involved become higher and higher or the corresponding distance scale becomes smaller and smaller, the latter refers to the fact that quarks do not exist in isolation and they exist only as colorless hadrons: mesons or baryons. While QCD has been extremely well tested at high energies by experiments where perturbation calculations can be carried out, an analytical solution to the QCD Lagrangian in the non-perturbative region is notoriously difficult and out of reach. As such our knowledge about how QCD works in the confinement region where the strong coupling constant is strong is rather poor. Nucleons, building blocks of atomic nuclei, which make up more than 99% of the visible matter in the universe, is a natural and an effective laboratory to study QCD in the confinement region. Hadron physics at low energies, particularly the structure of hadron (nucleon) has provided much insight about how QCD works in the confinement region.

The structure of nucleons is a rich, exciting and vibrant area of research, which involves studies of the ground state properties, their distributions as well as the excitation of the nucleons. Lepton scattering, particularly electron scattering has been proved a powerful microscope in probing the nucleon structure. It is a clean probe with the advantage of higher-order contributions being suppressed. With the development in polarized beam, recoil polarimetry, and polarized target technologies, polarization experiments have provided more precise data on quantities ranging from electromagnetic form factors of the nucleon [1, 2, 3] from elastic electron-nucleon scattering to spin structure functions [4] probed in deep inelastic lepton-nucleon scattering.

2 Electric and magnetic form factors of the nucleon and radii

Among quantities describing the structure of the nucleon, the electromagnetic form factors are the most fundamental quantities – they are sensitive to the distribution of charge and magnetization within the nucleon. At low four-momentum transfer squared Q^2 , they are sensitive to the pion cloud [5, 6, 7, 8, 9, 10], and provide tests of effective field theories of QCD based on chiral symmetry [11, 12]. Lattice QCD calculations continue to make advances in techniques [13, 14, 15] and computing power, and tests against precise nucleon form factor data will be possible in the future. Accurate measurements of nucleon electromagnetic form factors at low Q^2 are also important for the interpretation of parity-violation electron scattering experiments [16, 17], which probe the strange quark contribution to the nucleon electromagnetic structure. In the limit of $Q^2 \rightarrow 0$, the charge and magnetic radius of the nucleon can be determined from the slope of the corresponding electric and magnetic form factor. Precise information about the proton charge radius is particularly important because it is a crucial input to high precision tests of QED based on hydrogen Lamb shift measurements. The standard Lamb shift measurement probes the 1057 MHz fine structure transition between the $2S_{1/2}$ and $2P_{1/2}$ states in hydrogen. The hydrogen Lamb shift can be calculated to high precision from QED using higher order corrections. The proton rms charge radius is an important input in calculating the hadronic contribution to the hydrogen Lamb shift. The

subject of the charge radius of the proton has received a lot of attention recently because a new experiment reported [18] a much smaller value of the proton charge radius from a measurement of Lamb shift in muonic hydrogen atoms than the CODATA value [19] extracted from Lamb shift measurements of hydrogen atoms. The new experiment from muonic hydrogen Lamb shift has an unprecedented precision of 0.1%.

The experimental situation becomes more interesting as the latest value of the charge radius of the proton determined from an electron scattering experiment [20] is in agreement with the CODATA value [19]. The experiment [20] took place at the Mainz Microtron MAMI in which about 1400 cross sections from electron-proton elastic scattering were measured with negative four-momentum transfer squared, Q^2 values up to 1 (GeV/c)² with statistical uncertainties below 0.2%. The charge and magnetic radii of the proton were determined from this experiment from the extracted electric and magnetic form factors by fitting the cross section data to a variety of form factor models. They are:

$$\sqrt{\langle r_E^2 \rangle} = 0.879(5)_{\text{stat.}}(4)_{\text{syst.}}(2)_{\text{model}}(4)_{\text{group}} \text{ fm}$$

and

$$\sqrt{\langle r_M^2 \rangle} = 0.777(13)_{\text{stat.}}(9)_{\text{syst.}}(5)_{\text{model}}(2)_{\text{group}} \text{ fm.}$$

Figure 1 shows the results of the spline model for G_E and G_M and their ratio in a Q^2 region of 0 to 1.0 (GeV)² together with previous measurements and fits. Details about previous data and fits, as well as about other fits of the latest MAMI cross section data can be found in [20]. More recently, Zhan *et al.* [21] carried out a recoil polarization experiment in which the proton electric to magnetic form factor ratio was reported down to a Q^2 value of 0.3 (GeV/c)². These results show a different Q^2 dependence in the form factor ratio from that of the BLAST results [22] in a similar Q^2 range, in which a polarized internal hydrogen target was employed. Further experimental investigations are necessary to understand this difference. Zhan *et al.* [21] also reported an updated global fit of the form factors including their new data as well as other recent recoil polarization data [23, 24, 25] following the procedure of [26]. To extract the proton radii, they performed a fit by including data only up to $Q^2 = 0.5$ (GeV/c)² and the values they obtained are:

$$\sqrt{\langle r_E^2 \rangle} = 0.875(5) \pm 0.008_{\text{exp}} \pm 0.006_{\text{fit}} \text{ fm}$$

and

$$\sqrt{\langle r_M^2 \rangle} = 0.867(13) \pm 0.009_{\text{exp}} \pm 0.018_{\text{fit}} \text{ fm.}$$

Figure 2 shows a compilation of recent determination of the proton charge radius from hydrogen Lamb shift measurements [19], muonic hydrogen Lamb shift measurement [18], recent Mainz cross section measurement [20], and global analyses of electron scattering data [21, 27]. This highlights the large discrepancy between the result from the muonic hydrogen lamb shift measurement and those from all other measurements. The result from the muonic hydrogen Lamb shift is the most precise measurement to date and this large discrepancy needs a resolution by more theoretical investigations and new measurements.

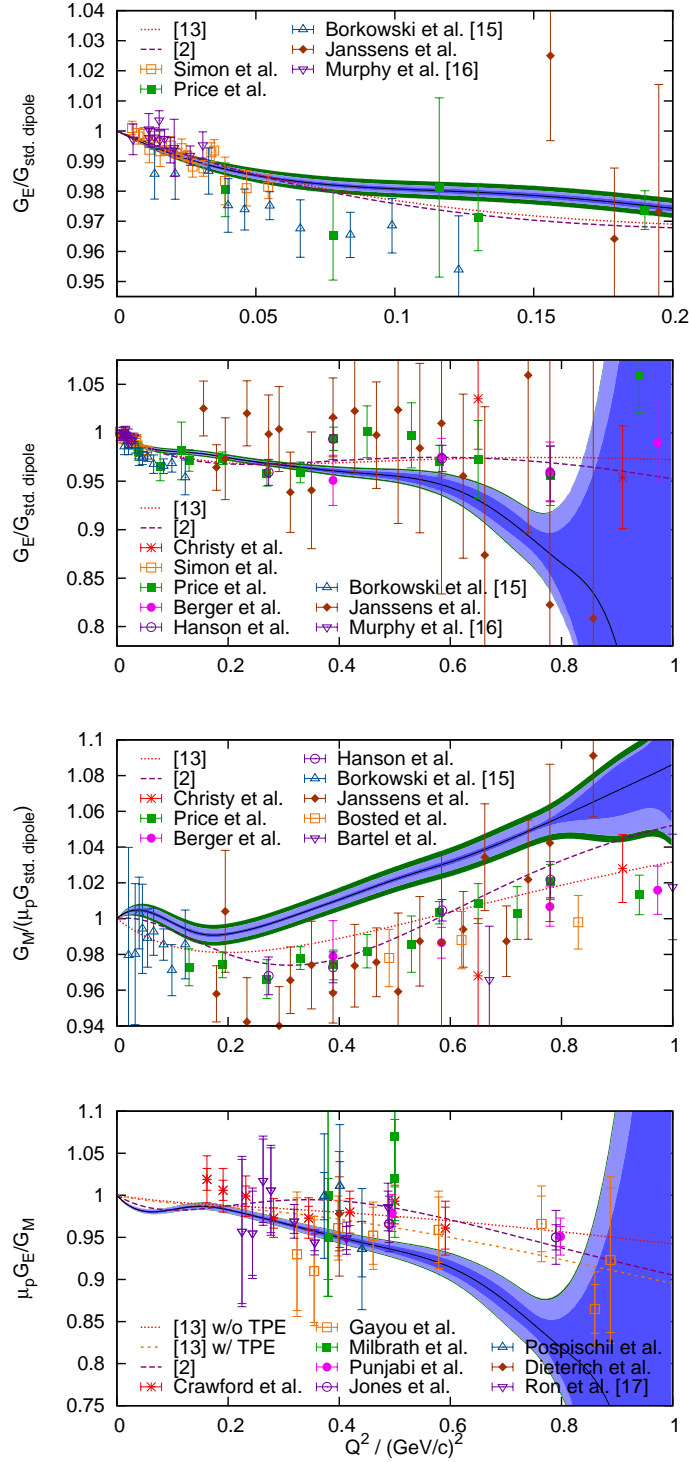


Figure 1: From [20]: The form factors G_E and G_M normalized to the standard dipole and G_E/G_M as a function of Q^2 . Black line: best fit to the data, blue area: statistical 68% pointwise confidence band, light blue area: experimental systematic error, green outer band: variation of the Coulomb correction by $\pm 50\%$. The different data points depict previous measurements, for Refs. see [6, 26]; we added the data points of [28, 29, 30]. Dashed lines are previous fits to the old data in [6, 26].

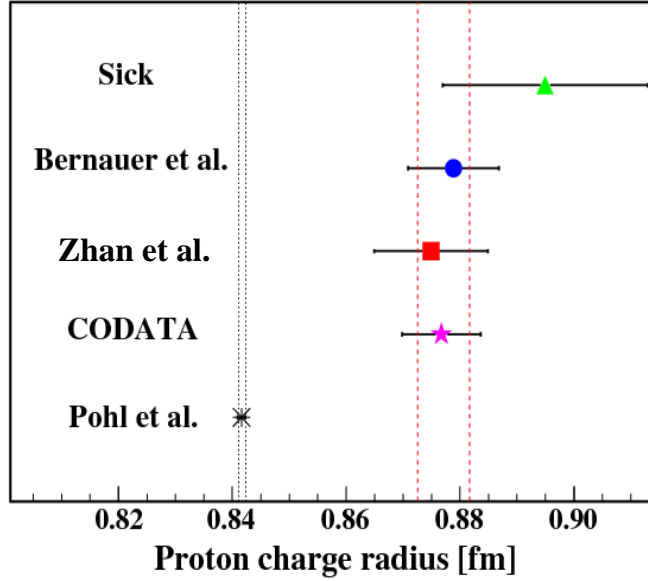


Figure 2: A compilation of recent measurements and analyses of proton rms charge radius from Zhan *et al.* [21]. Here “Zhan et al.” refers to the result from a global fit in [21].

3 Physics motivation

3.1 Proton charge radius from unpolarized $e - p$ elastic scattering

The elastic electron-nucleon scattering has proven to be a very useful tool for probing the structure of nucleons. The squared momentum transfer Q^2 carried by the exchanged virtual photon in elastic electron-proton (ep) scattering is defined in terms of the four-momenta of the incident and scattered electron; k and k' , respectively; by $Q^2 = -(k - k')^2$. By varying Q^2 , the spatial distributions of charge and current in the proton can be mapped and these charge and current distributions are related to the proton electric and magnetic Sachs form factors G_E^p and G_M^p .

In the low Q^2 region, below the two-pion production threshold; *i.e.*, $Q^2 < t_0$; $t_0 = (2m_\pi)^2 < 2 \text{ fm}^{-2}$; the energy transfer in the scattering process is negligible and the form factors can be taken as the Fourier transforms of the charge and current radial distributions $\rho_{\text{chg}}(r)$ and $\rho_{\text{cur}}(r)$.

The elastic electron-proton scattering can be described theoretically using the one-photon exchange approximation. In this model the cross section is written as:

$$\frac{d\sigma}{d\Omega}(E_0, \theta) = \sigma_{NS} \left(A(Q^2) + B(Q^2) \tan^2 \frac{\theta}{2} \right), \quad (1)$$

where σ_{NS} is the differential cross section for the elastic scattering from a point-like and spinless particle at incident energy E_0 and scattering angle θ . The two structure functions $A(Q^2)$ and $B(Q^2)$ are related to G_E^p and G_M^p by:

$$A(Q^2) = [G_E^p{}^2(Q^2) + \tau G_M^p{}^2(Q^2)] / (1 + \tau), \quad (2)$$

$$B(Q^2) = 2\tau G_M^p{}^2(Q^2), \quad (3)$$

with $\tau = Q^2 / (4M_p^2)$, where M_p is the proton mass.

Putting Eqs. 2 and 3 back into Eq. 1 we get the celebrated Rosenbluth formula [31]:

$$\frac{d\sigma}{d\Omega} = \left(\frac{d\sigma}{d\Omega} \right)_{\text{Mott}} \left(\frac{E'}{E} \right) \frac{1}{1 + \tau} \left(G_E^p{}^2(Q^2) + \frac{\tau}{\epsilon} G_M^p{}^2(Q^2) \right), \quad (4)$$

with the virtual photon longitudinal polarization parameter:

$$\epsilon = \left[1 + 2(1 + \tau) \tan^2 \frac{\theta}{2} \right]^{-1} \quad (5)$$

and the Mott structureless cross section:

$$\left(\frac{d\sigma}{d\Omega} \right)_{\text{Mott}} = \frac{\alpha^2 \left[1 - \beta^2 \sin^2 \frac{\theta}{2} \right]}{4k^2 \sin^4 \frac{\theta}{2}}, \quad (6)$$

where k^2 is the momentum of the incident electron.

In the case of small angles and very low Q^2 the contribution from the magnetic form factor, G_M^p , to the scattering process is suppressed and a precise separation of the two form factors using the Rosenbluth method [31] is no longer effective. On the other hand, at very low Q^2 values ($\sim 10^{-4}$) $(\text{GeV}/c)^2$, the uncertainty in extracting the electric form factor by neglecting the magnetic contribution from differential cross section measurement is significantly reduced, though precise measurements of differential cross sections at such low values of Q^2 are challenging.

At low Q^2 , the electric form factor of the proton can be expanded as:

$$G_E^p(Q^2) = 1 - \frac{Q^2}{6} \langle r^2 \rangle + \frac{Q^4}{120} \langle r^4 \rangle + \dots \quad (7)$$

Therefore, the root-mean-square (rms) charge radius of the proton is the slope of this expansion at $Q^2 \rightarrow 0$:

$$\frac{\langle r^2 \rangle}{6} = - \left. \frac{dG_E^p(Q^2)}{dQ^2} \right|_{Q^2=0}, \quad (8)$$

with the boundary condition $G_E^p(Q^2 = 0) = 1$. Therefore, to adequately determine the rms radius of the proton, high precision data of the proton form factors in the $Q^2 \rightarrow 0$ region are needed.

The two most precise and widely cited determinations of the proton charge radius in the literature before 2000 give $r_p = 0.805(11)$ fm [32] and $r_p = 0.862(12)$ fm [33], respectively, differing from each other by more than 7%. While precision hydrogen Lamb shift measurements [34, 35, 36, 37, 38] are in better agreement with the QED predictions using the smaller value of the proton charge radius without the two-loop binding effects, they are consistent with the larger value of the proton charge radius when two-loop binding effects are included in the QED calculations. We show that this discrepancy is dependent upon the data analysis and that the data are in fact consistent albeit with larger error bars.

Simon *et al.* [33] determined the proton charge radius by measuring the absolute differential cross sections of ep elastic scattering at Q^2 values from 0.14 fm^{-2} to 1.4 fm^{-2} . To extract G_E^p from the cross section measurement, they assumed the relation $G_M^p/\mu_p = G_E^p$. Their best fitted value, which also incorporated data from Orsay [39] and Saskatoon [29], gave the rms charge radius of the proton as $\langle r^2 \rangle^{1/2} = 0.862 \pm 0.12 \text{ fm}$. In their analysis G_E^p was assumed to have a

polynomial Q^2 dependence, so that $G_E^p = a_0 + a_1 Q^2 + a_2 Q^4$, neglecting terms higher than Q^4 . The effect of keeping the Q^6 term in the fit on the fitted value of $\langle r^2 \rangle^{1/2}$ was studied and found to be negligible. The other widely cited value for the proton rms charge radius before 2000 is from Hand *et al.* [32], which contains a compilation of data from different experiments. In their analysis, they also assumed that $\mu_p G_E^p = G_M^p$ and fitted G_E^p to the form $G_E^p = 1 - 1/6 \langle r^2 \rangle Q^2 + A Q^4$, using data for Q^2 up to 3 fm^{-2} to determine the parameter A . From this fit, they determined the rms charge radius of the proton to be $\langle r^2 \rangle^{1/2} = 0.805 \pm 0.011 \text{ fm}$.

In order to explore these discrepancies further, we re-fitted the G_E^p data from the experiments of Simon *et al.* and those compiled by Hand *et al.*. We concentrated on the data at the lowest values of Q^2 ($Q^2 < 2.0 \text{ fm}^{-2}$) in order to maintain a consistent range of data between these two analyses. Furthermore, the model-independent determination of the proton charge radius is especially sensitive to the data in the $Q^2 \rightarrow 0$ region, according to Eq. 8. In our analysis of the data from Hand *et al.* [32], in which we restricted the fit to include only those data with $Q^2 \leq 2.0 \text{ fm}^{-2}$, we obtained a proton charge radius, $\langle r^2 \rangle^{1/2} = 0.868 \pm 0.105 \text{ fm}$. When fitting the data compiled by Hand *et al.* up to 3.0 fm^{-2} , we obtained $\langle r^2 \rangle^{1/2} = 0.809 \pm 0.060 \text{ fm}$, essentially in agreement with Hand's published result of 0.805 fm . In fitting these data, the following functional form was used: $G_E^p = a_0 + a_1 Q^2 + a_2 Q^4$. Fitting the data from Mainz by Simon *et al.* [33] in the same way, we obtained $\langle r^2 \rangle^{1/2} = 0.878 \pm 0.024 \text{ fm}$, within errors of their published result of 0.862 fm . In addition to these two sets of data, we also re-analyzed the data from Höhler *et al.* [40] and we obtain $\langle r^2 \rangle^{1/2} = 0.863 \pm 0.057 \text{ fm}$, again within the consistent assumption concerning the ratio of the electric and magnetic form factors. Thus, these three determinations of the proton charge radius are consistent with one another within the errors. By restricting the data sets to the most sensitive Q^2 region, we were able to obtain consistent results from all three data sets at the expense of increased uncertainties in the extracted values of $\langle r^2 \rangle^{1/2}$.

The form-factor analysis of electron-proton scattering is based on one-photon exchange diagram. The validity of it is based on the assumptions that higher-order corrections are negligible. However, for any precision measurement as what is proposed here, it is important to address the higher-order electromagnetic corrections. Drell and Fubini [41] calculated the higher-order corrections and showed that the form factor analysis of electron-proton scattering is accurate to $\sim \frac{1}{137}$ for all angles and energies into the GeV range. They have used dispersion theory methods to formulate the electron-proton scattering amplitude in a manner which allows them to evaluate the e^4 contribution due to Compton scattering of the virtual intermediate photons by the proton.

Greenhut [42] calculated the two-photon exchange contribution to electron-proton scattering in second Born approximation using potentials representing the charge and magnetic moment distributions of the proton. The resonance contribution was calculated using a fit of the proton Compton scattering data. The numerical results showed that up to order α^3 , the two-photon exchange contribution is less than 0.8% at the kinematics (0.005 to 0.088 (GeV/c)^2) of the proposed BLAST experiment [48] in the case of the unexcited intermediate proton states and the resonance contribution at the kinematics of this experiment is negligible. Furthermore, one can follow the formalism derived by Greenhut to apply this correction to each Q^2 bin and the relative error from bin to bin due to this correction is negligible. For the proposed kinematics of this experiment, the effect is negligible.

Rosenfelder [43] applied the Coulomb correction to elastic electron-proton scattering and showed that the analysis of the electron scattering data including Coulomb correction lowers the χ^2 of the

fit and increase the proton radius by about (0.008 - 0.013) fm depending on the fit strategy. The Coulomb correction is calculated using a standard partial wave program which solves the Dirac equation in the electrostatic potential of the proton. The coulomb corrections are found to be small but positive, ranging from 0.4 - 0.9 %. These results are in good agreement with those from Greenhut, though in the latter case both the Coulomb and magnetic corrections have been taken into account using the second Born approximation.

A more recent extraction of the proton charge radius from a systematic analysis of the world unpolarized ep elastic scattering cross section data was carried out by Sick [27] in which Coulomb distortion correction and an electric form factor parametrization that allows for proper handling of higher moments have been adopted. The extracted value for the proton rms charge radius is 0.895 ± 0.018 fm. Most recently, Hill and Paz [44] carried out a model independent analysis of the electron scattering data using constraints from analyticity and obtained a proton rms charge radius of

$$r_p = 0.870 \pm 0.023 \pm 0.012 \text{ fm}$$

using just proton scattering data.

3.2 Double-polarization $e - p$ elastic scattering and proton charge radius

Interference between G_E^p and G_M^p provides an easily measurable asymmetry when using a beam of polarized electrons in concert with a polarized proton target or a recoil proton polarimeter. A combination of a double-spin asymmetry measurement and unpolarized differential cross section measurement in ep elastic scattering in principle allows for a good separation of the two form factors.

In the one-photon-exchange Born approximation, the elastic scattering of longitudinally polarized electrons from unpolarized protons results in a transfer of polarization to the recoil proton with only two non-zero components: P_t perpendicular to, and P_l parallel to the proton momentum in the scattering plane [45]. The form factor ratio can be determined from a simultaneous measurement of the two recoil polarization components in the scattering plane:

$$\frac{G_E^p}{G_M^p} = -\frac{P_t}{P_l} \frac{E + E'}{2M} \tan\left(\frac{\theta}{2}\right), \quad (9)$$

where E and E' are the incident and scattered electron energy, respectively, and θ is the electron scattering angle. Most recently, this technique has been used in a number of experiments at Jefferson Lab [21, 23, 24, 25], and also in an upcoming experiment [46] from a Q^2 value of 0.7 down to $0.25 (\text{GeV}/c)^2$.

In the one-photon exchange approximation, the elastic scattering asymmetry of longitudinally polarized electrons from polarized protons with respect to the electron beam helicity has the form [47]

$$A_{\text{phys}} = \frac{v_z \cos \theta^* G_M^{p^2} + v_x \sin \theta^* \cos \phi^* G_M^p G_E^p}{(\tau G_M^{p^2} + \epsilon G_E^{p^2}) / [\epsilon(1 + \tau)]}, \quad (10)$$

where θ^* and ϕ^* are the polar and azimuthal angles of the target polarization defined relative to the three-momentum transfer vector of the virtual photon and $\tau = Q^2/(4M_p^2)$ with the proton mass M_p . The longitudinal polarization of the virtual photon is denoted as $\epsilon = [1 + 2(1 + \tau) \tan^2(\theta_e/2)]^{-1}$

where θ_e is the electron scattering angle, and $v_z = -2\tau \tan(\theta_e/2) \sqrt{1/(1+\tau) + \tan^2(\theta_e/2)}$, $v_x = -2 \tan(\theta_e/2) \sqrt{\tau/(1+\tau)}$ are kinematic factors. The experimental asymmetry

$$A_{\text{exp}} = P_b P_t A_{\text{phys}} \quad (11)$$

is reduced by the beam (P_b) and target (P_t) polarizations. A determination of the ratio $\frac{G_E^p}{G_M^p}$, independent of the knowledge of the beam and target polarization, can be precisely obtained by forming the so-called super ratio [1]:

$$R = \frac{A_1}{A_2} = \frac{2\tau v_{T'} \cos \theta_1^* G_M^p{}^2 - 2\sqrt{2\tau(1+\tau)} v_{TL'} \sin \theta_1^* \cos \phi_1^* G_M^p G_E^p}{2\tau v_{T'} \cos \theta_2^* G_M^p{}^2 - 2\sqrt{2\tau(1+\tau)} v_{TL'} \sin \theta_2^* \cos \phi_2^* G_M^p G_E^p}, \quad (12)$$

where A_1 and A_2 are elastic electron-proton scattering asymmetries measured at the same Q^2 value, but two different proton spin orientations relative to the corresponding three-momentum transfer vector, *i.e.*, (θ_1^*, ϕ_1^*) and (θ_2^*, ϕ_2^*) , respectively.

For a detector configuration that is symmetric with respect to the incident electron momentum direction, A_1 and A_2 can be measured simultaneously by forming two independent asymmetries with respect to either the electron beam helicity or the target spin orientation in the beam-left and beam-right sector of the detector system, respectively. The target spin direction would be chosen to optimize the determination of the proton form factor ratio given the experimental running conditions and the running time. This technique was pioneered in the BLAST experiment at MIT-Bates [22], and a proposal based on this technique for a precision measurement of the proton charge radius was conditionally approved [48] at Bates in late 1990s. This technique will also be used in the upcoming experiment [46] from a Q^2 value of 0.4 down to 0.015 (GeV/c)² using a dynamically polarized NH₃ target [49, 50].

3.3 Proton charge radius from atomic measurements

As we mentioned previously, precision tests of QED calculations of hydrogen Lamb shift with higher orders require precise information on the rms charge radius of the proton. However, the current situation from electron scattering on the proton charge radius discussed previously has not quite reached the level which can make a major impact on high precision test of QED. On the other hand, the precision of hydrogen Lamb shift measurements has improved significantly in the last two decades or so, particularly with the advancement of optical measurements [34, 51, 35, 36, 37, 38, 52]. As such, the rms charge radius of the proton can be extracted by the combination of hydrogen Lamb shift measurements and state-of-the-art QED calculations [53]. The CODATA [19] recommended value for the proton rms charge radius from hydrogen Lamb shift is

$$r_p = 0.8768 \pm 0.0069 \text{ fm.}$$

This value is in good agreement from the values reported by Bernauer *et al.* [20], and Zhan *et al.* [21]. For a review of hydrogen Lamb shift measurements, we refer readers to [54].

The sensitivity to the proton charge radius is further enhanced by measuring the Lamb shift of muonic hydrogen atom due to the fact that muon is about a factor of 200 more massive compared to electron. Such measurements, however, are very challenging and have taken a long time to

succeed. Last year, a collaboration at PSI reported [18] the most precise value of the proton charge radius from a measurement of muonic hydrogen Lamb shift. The reported value of the proton charge radius is

$$r_p = 0.84184 \pm 0.00067 \text{ fm}$$

which has a relative precision of better than 0.1%. However, this value is 5σ away from the CODATA value determined from the hydrogen Lamb shift measurements. It is also much smaller than most values reported from electron scattering experiments and analyses with the exception of a dispersion analysis of electron scattering data by Belushkin *et al.* [55], in which a value in the range of 0.822 to 0.852 fm has been obtained for the proton rms charge radius.

3.4 Summary

The PSI result caused a lot of excitement and also raised many questions. Is there a problem with proton size? Is new physics discovered [56]? What effects are missing in state-of-the-arts calculations [57, 58]? Are there additional corrections to the muonic Lamb shift due to the structure of the proton [59, 60]? Are the higher moments of the charge distribution taken into account correctly in the extraction of the proton rms charge radius [61, 62, 63, 64, 65, 66, 67]? However, so far there is no resolution or reconciliation about the discrepancy between values of the proton charge radius extracted between the electronic and muonic hydrogen Lamb shift measurements.

The current discrepancy in the values of the proton charge radius extracted from experiments using three different techniques strongly suggests the importance and urgency to carry out a new measurement which relies on a different technique. Here we propose to perform a new, magnetic-spectrometer-free electron scattering experiment using a calorimeter with normalizing the ep cross sections to that of the well known $e^-e^- \rightarrow e^-e^-$ Møller process.

4 Proposed experiment

In this proposal we are suggesting to perform a new electron scattering experiment on hydrogen ($ep \rightarrow ep$) at small angles to address the current “*proton charge radius crisis*”. The suggested experiment will be done with a calorimetry method as opposed to most of the previous ep experiments using the traditional magnetic spectrometers. The proposed experimental apparatus will include:

- (1) a windowless gas flow hydrogen target;
- (2) a package of detectors for the scattered electrons including a multi-channel high resolution and high acceptance PbWO_4 calorimeter located at 5-8 m downstream from the gas target (see Sec. 5).

The suggested experimental design will allow detection of the scattered electrons to angles as low as $\sim 0.5^\circ$ level, never reached before by magnetic spectrometer measurements. Also, with its high acceptance and azimuthally symmetric capabilities, the setup will simultaneously detect multi-electron processes like the Møller scattering.

4.1 Major advantages of the proposed experiment

This experiment will have three major improvements over previous electron scattering experiments:

- (1) The ep cross sections will be normalized to the well known QED process - Møller scattering, which will be measured simultaneously during the experiment within the same detector acceptance. This, arguably, will be a superior method to control the systematic uncertainties in the $ep \rightarrow ep$ cross sections.
- (2) The suggested non-magnetic and calorimetric experiment will have a good possibility to reach the extreme forward angles for the first time in ep scattering experiments. The suggested experimental setup will cover the very forward angles ($\sim 0.5^\circ - 4^\circ$), which in turn will allow to reach extremely low Q^2 range ($10^{-4} - 10^{-2}$) $(\text{GeV}/c)^2$ for few GeV incident electron beams. The lowest Q^2 range measured up to date is the recent Mainz experiment [20] where the minimum value for Q^2 reached is $3 \cdot 10^{-3} (\text{GeV}/c)^2$. Including this very low Q^2 range is critically important since the rms charge radius of the proton is being extracted as the slope of the measured $G_E^p(Q^2)$ at the $Q^2=0$ point (see Eq. 8). We also understand that in going to very small Q^2 range, one has to take care of the uncertainties in the measured cross sections and Q^2 , as well as still provide a reasonably large interval of Q^2 to facilitate the extraction of the slope from G_E^p vs. Q^2 dependence.

In this proposed experiment we suggest to reach the highest precision in measuring the cross sections by continuously measuring the Møller scattering process and using different energy values for the incident electron beam to cover a sufficient range in Q^2 ($10^{-4} - 10^{-2}$) $(\text{GeV}/c)^2$.

In order to achieve these objectives we propose to run at two different beam energies, which will ensure coverage of a large enough range in Q^2 and also provide significant overlap in

the Q^2 range for systematic studies. This will also help to control the systematics of the radiative correction calculations.

- (3) We propose to use a windowless gas flow target in this experiment. This will sufficiently cut down the experimental background from the target windows which is typical for all previous ep experiments. With this type of gas target the absolute majority of events in the PbWO_4 calorimeter will be produced by the two processes: $ep \rightarrow ep$ and $e^-e^- \rightarrow e^-e^-$, both of which are the direct interests in this proposed experiment.

The calorimeter proposed for this experiment (see Sec. 5.4), with high resolution PbWO_4 crystal detectors located in the beamline with a $4 \times 4 \text{ cm}^2$ hole in the central part, will allow a direct and simultaneous detection of both $ep \rightarrow ep$ and $e^-e^- \rightarrow e^-e^-$ processes. The trigger in this experiment (total energy deposited in calorimeter $\geq 20\%$ of E_0 , as described in Sec. 5.6) will allow for the detection of the Møller events in both single-arm and double-arm modes. In the case of double-arm mode, already two selection criteria, the co-planarity and elasticity in energy (described in Sec. 6.2.2) will provide a good event selection in this very low background experiment.

The $ep \rightarrow ep$ elastic cross sections in this proposed experiment will be normalized to $e^-e^- \rightarrow e^-e^-$ Møller cross sections, which can be calculated with sub-percent accuracy ($\sim 0.5\%$) within the QED framework, including the radiative corrections.

The experimental differential cross sections for $ep \rightarrow ep$ scattering are written as:

$$\left(\frac{d\sigma}{d\Omega}\right)_{ep}(Q_i^2) = \frac{N_{\text{exp}}^{\text{yield}}(ep \rightarrow ep \text{ in } \theta_i \pm \Delta\theta)}{N_{\text{beam}}^{e^-} \cdot N_{\text{tgt}}^{\text{H}} \cdot \varepsilon_{\text{geom}}^{ep}(\theta_i \pm \Delta\theta) \cdot \varepsilon_{\text{det}}^{ep}}. \quad (13)$$

On the other hand, the differential cross sections for the Møller process, measured simultaneously in this experiment, will have a similar dependence on the experimental quantities:

$$\left(\frac{d\sigma}{d\Omega}\right)_{e^-e^-} = \frac{N_{\text{exp}}^{\text{yield}}(e^-e^- \rightarrow e^-e^-)}{N_{\text{beam}}^{e^-} \cdot N_{\text{tgt}}^{\text{H}} \cdot \varepsilon_{\text{geom}}^{e^-e^-} \cdot \varepsilon_{\text{det}}^{e^-e^-}}, \quad (14)$$

where $N_{\text{exp}}^{\text{yield}}(ep \rightarrow ep \text{ in } \theta_i \pm \Delta\theta)$ is the number of elastically scattered $ep \rightarrow ep$ events inside a particular azimuthally symmetric ring on PbWO_4 with polar angles in $(\theta_i \pm \Delta\theta)$ range which defines the $Q_i^2 \pm \Delta Q^2$ for a fixed incident energy (see Fig. 3); $N_{\text{exp}}^{\text{yield}}(e^-e^- \rightarrow e^-e^-)$ is the same quantity as for ep , defined in three different ways described below; $N_{\text{beam}}^{e^-}$ is the number of beam electrons that passed through the target with the number of H atoms/cm² - $N_{\text{tgt}}^{\text{H}}$, during the measurement; $\varepsilon_{\text{geom}}^{ep}(\theta_i \pm \Delta\theta)$ is the geometrical acceptance of the $(\theta_i \pm \Delta\theta)$ ring for the $ep \rightarrow ep$ reaction; $\varepsilon_{\text{geom}}^{e^-e^-}$ is the same for the $e^-e^- \rightarrow e^-e^-$ process and it will be calculated in three different ways depending on the accepted method for the Møller process, and it is described below; $\varepsilon_{\text{det}}^{ep}$ and $\varepsilon_{\text{det}}^{e^-e^-}$ are the detection efficiencies of the particular elements of the setup for the scattered electrons.

The ratio of Eqs. 13 to 14 will relate the ep cross sections relative to the e^-e^- Møller cross sections:

$$\left(\frac{d\sigma}{d\Omega}\right)_{ep}(Q_i^2) = \left[\frac{N_{\text{exp}}^{\text{yield}}(ep \rightarrow ep \text{ in } \theta_i \pm \Delta\theta)}{N_{\text{exp}}^{\text{yield}}(e^-e^- \rightarrow e^-e^-)} \cdot \frac{\varepsilon_{\text{geom}}^{e^-e^-}}{\varepsilon_{\text{geom}}^{ep}} \cdot \frac{\varepsilon_{\text{det}}^{e^-e^-}}{\varepsilon_{\text{det}}^{ep}} \right] \left(\frac{d\sigma}{d\Omega}\right)_{e^-e^-}. \quad (15)$$

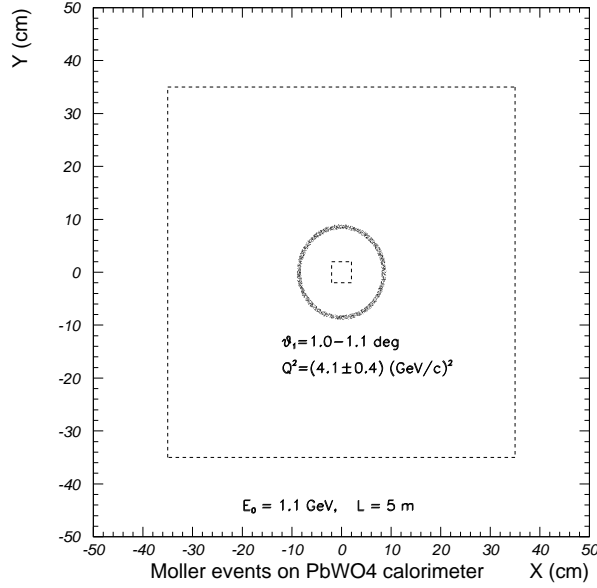


Figure 3: The $X - Y$ position distribution of a single Møller scattered electron in the calorimeter at $E_0 = 1.1$ GeV. The angular range of the detected electron is $\theta_1 = 1.0^\circ - 1.1^\circ$ giving a Q^2 range of $Q^2 = (4.1 \pm 0.4) \cdot 10^{-4} (\text{GeV}/c)^2$.

Right away, the two major sources of systematic uncertainties, N_{beam}^e and N_{tgt}^H , in the above ratio which dominated in the previous experiments are simply canceling out in this proposed experiment.

The remaining two sources of systematic uncertainties: the ratio of the geometrical uncertainties $(\varepsilon_{\text{geom}}^{e^-e^-} / \varepsilon_{\text{geom}}^{ep})$ and the detection efficiency $(\varepsilon_{\text{det}}^{e^-e^-} / \varepsilon_{\text{det}}^{ep})$ will have a different impact on the final systematic uncertainties depending on the selection method of the Møller events.

4.2 Møller event selection methods

We are planning to use three different approaches for the identification of the Møller events to reduce systematics in precise determination of the Møller scattering process.

4.2.1 Single-arm Møller event selection method

The proposed experimental setup (see Sec. 5) is optimized in a way that both Møller scattered electrons will be detected in the calorimeter for angles $\geq 0.7^\circ$ (see Sec. 6.2.2). However, looking at Eq. 15 for the case when one defines the Møller process inside the same angular $(\theta_i \pm \Delta\theta)$ ring (see Fig. 3) with one of the scattered electrons detected (single-arm Møller method), then we get $\varepsilon_{\text{geom}}^{ep} = \varepsilon_{\text{geom}}^{e^-e^-}$ and $\varepsilon_{\text{det}}^{ep} = \varepsilon_{\text{det}}^{e^-e^-}$ having in mind the different energy values of these electrons. With that, Eq. 15 becomes:

$$\left(\frac{d\sigma}{d\Omega} \right)_{ep} (Q_i^2) = \left[\frac{N_{\text{exp}}^{\text{yield}} (ep \rightarrow ep \text{ in } \theta_i \pm \Delta\theta)}{N_{\text{exp}}^{\text{yield}} (e^-e^- \rightarrow e^-e^-)} \right] \left(\frac{d\sigma}{d\Omega} \right)_{e^-e^-} \quad (16)$$

and, therefore, allows for a determination of the ep scattering cross sections essentially without systematic uncertainties related to the experimental apparatus.

Since the $e^-e^- \rightarrow e^-e^-$ is a two-body reaction, the experimental scattering angle of one of the electrons, together with the well known ($\Delta E/E = 10^{-4}$) incident beam energy will define the kinematics of the process. With that, the measured energy in the calorimeter (E_{meas}) can be used to select the events in the experiment. Figure 4 demonstrates that a good resolution in the reconstructed energy ($E_{\text{rec}} - E_{\text{meas}}$) will give a high level of confidence that this selection criterion alone will allow for an effective selection of events in this low-background experiment. Figure 5 also demonstrates the effective separation of Møller events from the ep elastic scattered events for angles $\theta_e > 0.7^\circ$ that is planned for this experiment.

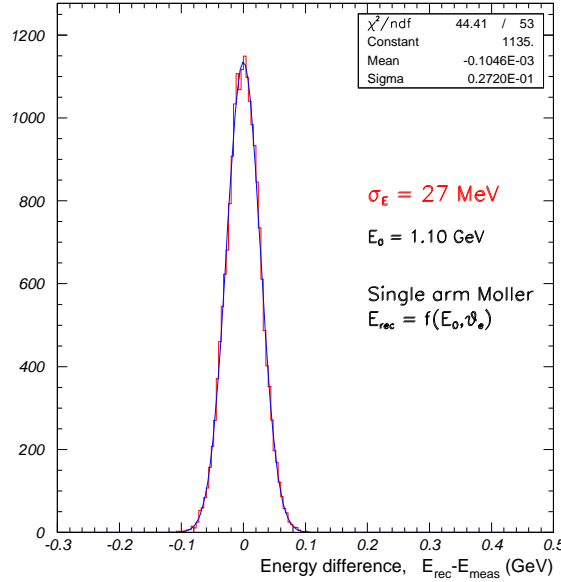


Figure 4: The resolution of the reconstructed and the measured energies ($E_{\text{rec}} - E_{\text{meas}}$) for detecting a single Møller scattered electron in the calorimeter at $E_0 = 1.1$ GeV and $\theta_e > 0.7^\circ$.

4.2.2 Coincident event selection method

As already mentioned above, the proposed experiment is optimized in a way that both electrons from $e^-e^- \rightarrow e^-e^-$ will be detected in the calorimeter for angles $\theta_e > 0.7^\circ$. We will also explore the selection of Møller events in coincidence. As illustrated in Fig. 6, this method, in addition to the same Q_i^2 ring ($\theta_i \pm \Delta\theta$), will introduce a second ring on the calorimeter for the detection of the second Møller scattered electron. As a consequence, it may introduce different geometrical acceptances and detection efficiencies for the particular Q^2 which can be calculated by Monte Carlo simulations and tested by the extracted Møller cross sections.

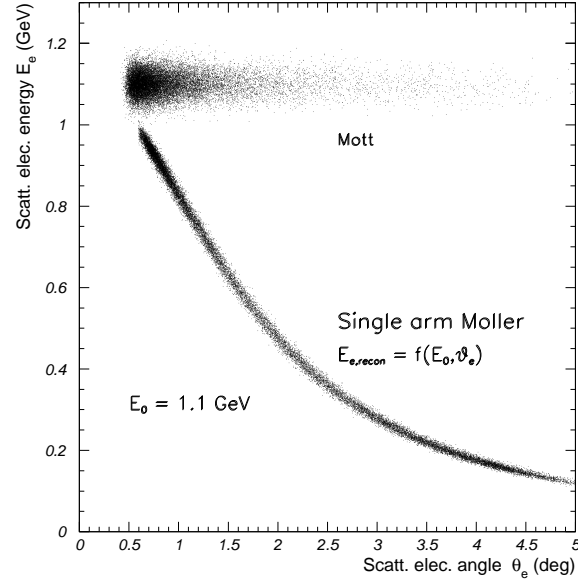


Figure 5: The energy vs. scattering angle distribution of $e-p$ elastic and one of the Møller scattered electrons at $E_0 = 1.1$ GeV.

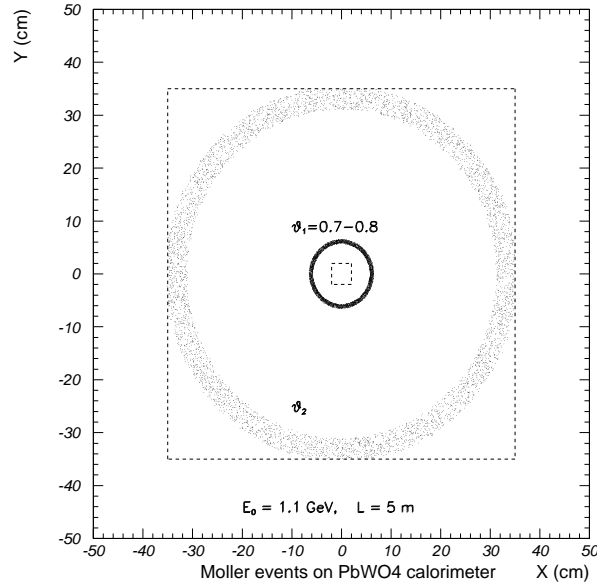


Figure 6: The $X - Y$ position distribution of the the two Møller scattered electrons on the PbWO_4 calorimeter at a distance of 5 m from the target at an incident beam energy of 1.1 GeV. The distribution of the second electron is shown as the outer ring θ_2 when the first electron is in the range $\theta_1 = 0.7^\circ - 0.8^\circ$. The outside square box is the size of the PbWO_4 calorimeter.

4.2.3 Integrated Møller cross section method

In this case, we will normalize the ep cross sections to the Møller cross sections extracted from the entire fiducial volume of the calorimeter for all Q^2 values. With that, Eq. 15 becomes:

$$\left(\frac{d\sigma}{d\Omega}\right)_{ep}(Q_i^2) = \left[\frac{N_{\text{exp}}^{\text{yield}}(ep, \theta_i \pm \Delta\theta)}{N_{\text{exp}}^{\text{yield}}(e^-e^-, \text{ on PbWO}_4)} \right] \frac{\varepsilon_{\text{geom}}^{e^-e^-}(\text{all PbWO}_4)}{\varepsilon_{\text{geom}}^{ep}(\theta_i \pm \Delta\theta)} \frac{\varepsilon_{\text{det}}^{e^-e^-}(\text{all PbWO}_4)}{\varepsilon_{\text{det}}^{ep}(\theta_i \pm \Delta\theta)} \cdot \left(\frac{d\sigma}{d\Omega}\right)_{e^-e^-}, \quad (17)$$

with $\left(\frac{d\sigma}{d\Omega}\right)_{e^-e^-}$ integrated over the PbWO_4 calorimeter acceptance.

4.3 Relation to other experiments

The other experiment that is related to this proposed experiment is the ‘‘Measurement of the Proton Elastic Form Factor Ratio at Low Q^2 ’’ (E08-007) [68] which is currently scheduled to run in Hall A in January, 2012. In E08-007 the electric to magnetic form factor ratio, G_E/G_M , will be studied in the range of $Q^2 = 0.015 - 0.7 \text{ (GeV/c)}^2$ with sub-percent precision. The results of this experiment will greatly improve the knowledge of the ratio in this Q^2 range, which, in combination with separate cross section data, will also allow significant improvements in the knowledge of the individual form factors. However, in our proposed experiment the electric form factor, G_E^p , will be measured directly in the very low Q^2 range of $2 \cdot 10^{-4} - 2 \cdot 10^{-2} \text{ (GeV/c)}^2$ which will allow a definitive extraction of the proton charge radius with sub-percent precision.

5 Experimental apparatus

5.1 Introduction

The proposed experiment plans to use an existing high resolution and high efficiency PbWO_4 crystal electromagnetic calorimeter together with a windowless gas flow hydrogen target to detect the scattered electrons from *ep* elastic and Møller scatterings with high precision. A windowless target cell has a definitive advantage over closed cell targets in minimizing one of the primary sources of background compared to previous measurements of the same reactions. The scattered electrons travel through a large area vacuum box with thin windows to minimize multiple scattering and backgrounds. The vacuum box matches the geometrical acceptance of the calorimeter. The PbWO_4 calorimeter is preceded by a set of $X-Y$ scintillator veto counters for minimizing neutral particle backgrounds from the target.

The elements of the experimental apparatus along the beamline are as follows:

- windowless gas flow hydrogen target
- vacuum box with only one thin window at the calorimeter end
- $X-Y$ veto counters
- high resolution PbWO_4 crystal calorimeter

Figure 7 shows a schematic layout of the experimental setup.

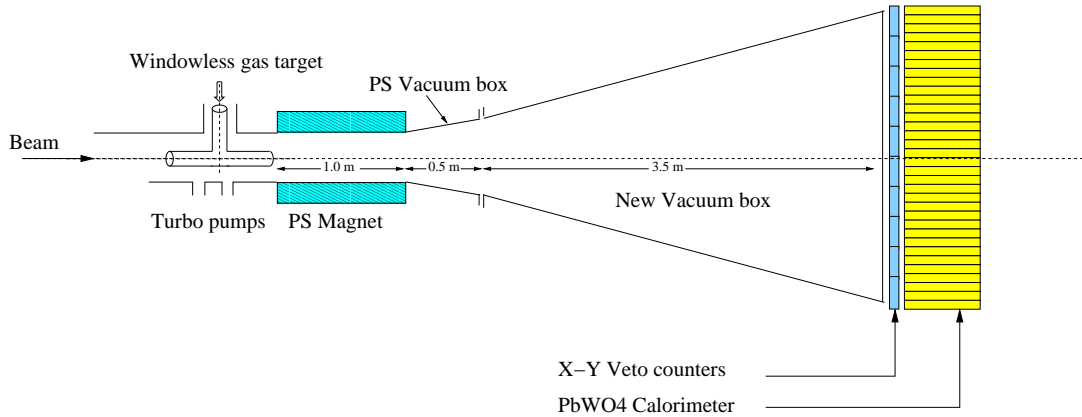


Figure 7: Schematic layout (not to scale) of the experimental apparatus to measure the proton charge radius.

5.2 Electron beam

The electron beam parameters, such as energy, polarization, intensity and size, required for the proton charge radius measurement are all within the Hall B beam specifications, as shown in Table 1.

A critical component of this proposed experiment is a windowless gas flow hydrogen target having a thickness of about $\sim 1 \times 10^{18}$ hydrogen atoms/cm². With an incident beam current of 10 nA, this gives a luminosity of about $\mathcal{L} \approx 6 \times 10^{28}$ cm⁻² s⁻¹.

Table 1: CEBAF beam parameters in the proton charge radius measurement.

Experiment	Energy (GeV)	Polarization	Current (nA)	Size (rms) (mm)
proton charge radius	1.1, 2.2	none	10	~ 0.08

5.3 Windowless gas flow target

In order to achieve the expected rates of Møller scattered electrons in this experiment (see Sec. 9) with an incident electron beam current of 10 nA, a target thickness of $t \sim 1 \times 10^{18}$ hydrogen atoms/cm² is required. We propose to generate the target thickness by flowing cold hydrogen gas through a small diameter thin-walled cylindrical tube open at both ends. Such a windowless target cell has the definitive advantage over closed cell targets in minimizing the overall background in the experiment. As noted in the recent precision measurements of elastic ep scattering cross sections from MAMI at Mainz [20], the primary source of background was the elastic and quasielastic scattering off the nuclei in the walls of the closed-cell target.

The target cell envisaged for this proton charge radius measurement is based on the proposed DarkLight [69] experiment at Jefferson Lab with the FEL beam. The gas flow target consists of a horizontal cylindrical cell pressurized to a pressure p_1 at a temperature T_1 by a constant inlet feed. The gas flows out into the beam pipe vacuum through two small conductance tubes of half-length $L/2$ and diameter D concentric to the beam axis upstream and downstream of the cell. Since there is no appreciable back pressure from the beam vacuum, the gas exits at near the speed of sound in the absence of a special Laval nozzle at the tube exit. Similar gas flow targets are currently in use for the OLYMPUS [70] experiment at DORIS/DESY and have been used for the HERMES [71] experiment at HERA/DESY.

For low pressures (molecular flow) the conductance, C (l/s), of a tube of uniform circular cross section with diameter D (cm), length L (cm) is given by [72]

$$C = 3.81 \frac{D^3}{L} \sqrt{\frac{T}{M}} \quad (18)$$

where T is the temperature and M is the mass number of the gas.

The mass flow rate, Q , of a gas through an outflow tube expressed in terms of volume flow normalized to a temperature T_0 times the gas pressure is:

$$Q = \frac{\pi}{4} D \text{Re} \mu R \frac{T_0}{M} \quad (19)$$

where R is the universal gas constant, Re is the Reynolds number, μ is the dynamic viscosity of the gas. Thus, for a given Q and μ , the Reynolds number and Mach number η_1 can be determined from which, for a given cell temperature T_1 , the cell pressure p_1 can be calculated. The resulting target thickness $t = \rho L$, where ρ is the particle density and L is the target length, is

$$\begin{aligned} t &= \frac{N_A}{V_{\text{mol}}} L \frac{p_1}{736 \text{ Torr}} \frac{273 \text{ }^\circ\text{K}}{T_1} \\ &= 1.00 \times 10^{19} \frac{L}{\text{cm}} \frac{p_1}{\text{Torr}} \frac{^\circ\text{K}}{T_1} \end{aligned} \quad (20)$$

The specific hydrogen target proposed for the proton charge radius experiment is a thin-walled (30 μm thick) Kapton tube with the following dimensions and parameters:

$$L = 4 \text{ cm}; \quad D = 4 \text{ mm}; \quad \rho_0 = 2.5 \times 10^{17} \text{ H}_2/\text{cm}^3 \text{ (initial density at target center)}.$$

With these parameters one finds

$$\eta_1 \approx 0.3; \quad \text{Re} \approx 207; \quad p_1 \approx 6.8 \text{ Torr}.$$

The total particle flux through both ends of the target cell is $\varphi = \rho_0 C \approx 2.2 \times 10^{20} \text{ H}_2/\text{s}$ for a mass flow rate of $Q \approx 6.3 \text{ Torr-l/s}$ at $T_1 = 25^\circ \text{K}$. The gas flow remains laminar ($\text{Re} \leq 1200$) up to mass flow of $Q = 150 \text{ Torr-l/s}$. Over an average length of about 1.5 cm for a triangular shaped density profile along the target length, a flow rate of $Q \approx 6.3 \text{ Torr-l/s}$ can produce the required thickness of $\sim 10^{18}$ hydrogen atoms/cm². A schematic of the principle of the proposed windowless gas flow target is shown in Fig. 8 and the target parameters are listed in Table 2.

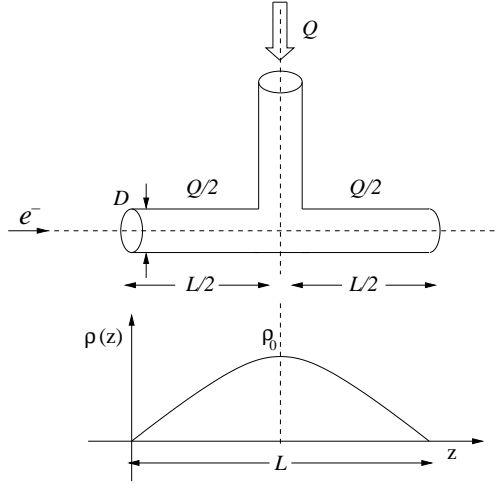


Figure 8: The principle of the windowless gas flow target. Hydrogen gas flows at a rate of Q Torr-l/s into the cell and exits symmetrically along conductance tubes of length $L/2$ and inner diameter D . The density profile along the target cell is approximately triangular.

Table 2: Windowless H_2 gas flow target parameters for the proton charge radius measurement.

H thickness (atoms/cm ²)	$t = 10^{18}$
Cell wall (Kapton) thickness (μm)	30
Cell diameter (cm)	$D = 0.4$
Cell length (cm)	$L = 4.0$
Inlet gas temperature ($^\circ\text{K}$)	$T = 25$
Gas pressure at target center (Torr)	$P_0 = 6.8$
Mass flow rate (Torr-l/s)	$Q = 6.3$

A three-stage differential pumping system on both the upstream and downstream ends of the target cell will be required to pump away the residual gas and interface to the $\approx 5 \times 10^{-6}$ Torr

vacuum pressure of the beamline. This can be achieved with magnetically levitated turbo molecular pumps with high pumping speeds (~ 2800 l/s for H_2) capable of approximately 10^2 reduction in pressure at each of the three pumping stages.

5.4 High resolution forward calorimeter

The scattered electrons from $e-p$ elastic and Møller scatterings in this precision experiment will be detected with a high resolution and high efficiency electromagnetic calorimeter. In the past decade, lead tungstate ($PbWO_4$) has become a popular inorganic scintillator material for precision compact electromagnetic calorimetry in high and medium energy physics experiments (CMS, ALICE at the LHC) because of its fast decay time, high density and high radiation hardness. Recently, the PrimEx Collaboration at Jefferson Lab has constructed a novel state-of-the-art multi-channel electromagnetic hybrid ($PbWO_4$ -lead glass) calorimeter (HYCAL) [75] to perform a high precision (1.5%) measurement of the neutral pion lifetime via the Primakoff effect.

The $PbWO_4$ central insertion part of HYCAL will be used as the calorimeter for this experiment. A single $PbWO_4$ module is 2.05×2.05 cm² in cross sectional area and 18.0 cm in length ($20X_0$). The calorimeter consists of 1152 modules arranged in a 34×34 square matrix (70×70 cm² in size) with four crystal detectors removed from the central part (4.1×4.1 cm² in size) for passage of the incident electron beam. Figure 9 shows the assembled PrimEx HYCAL calorimeter. The calorimeter will be at a distance of about 5 m from the target which will provide a geometrical acceptance of about 25 msr.

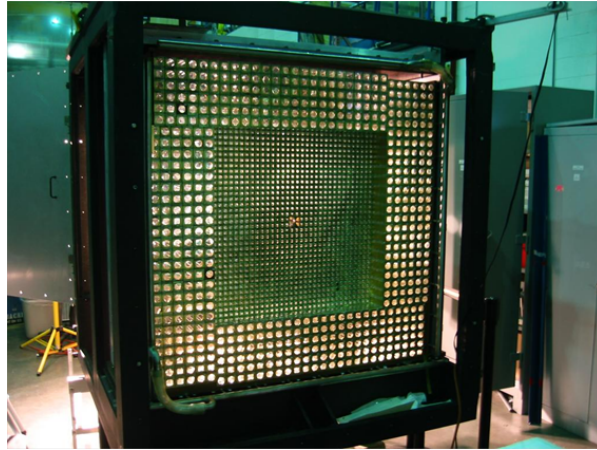


Figure 9: The PrimEx HYCAL calorimeter with all modules of the high performance $PbWO_4$ crystals in place.

The performance characteristics of the $PbWO_4$ crystals are well known mostly for high energies (>10 GeV) [73] and at energies below one GeV [74]. In order to check the performance of the PrimEx calorimeter crystals with few GeV electron/photon beams, tests were carried out with a 6×6 prototype crystal detector. As the light yield of the crystal is highly temperature dependent ($\sim 2\%/^{\circ}C$ at room temperature), the detector array was maintained at a stable temperature of $T = 4 \pm 0.1^{\circ}C$ during the tests. For finer definition of the impact coordinates of the electrons on the crystal array, a pair of $X-Y$ array of scintillating fibers with a fiber-width of 0.2 cm was used in front of the calorimeter.

5.4.1 Energy resolution

The energy calibration of the PbWO_4 crystal part of HYCAL was performed with 4 GeV electrons irradiating the centers of each crystal module. The reconstructed energy distribution of is shown in Fig. 10 for three different calibrated energy sums: the central single module; the inner section comprising of a 3×3 array; and the total array of 6×6 crystals. The central module already contains $\sim 75\%$ of the total energy deposition. An excellent energy resolution of $\sigma_E/E = 2.6\%/\sqrt{E}$ has been achieved by using a Gaussian fit of the line-shape obtained from the 6×6 array. After subtraction of the beam energy spread due to the finite size of the scintillating fiber, as well as multiple scattering effects in vacuum windows and in air, a level of 1.2% energy resolution was reached for 4 GeV electrons.

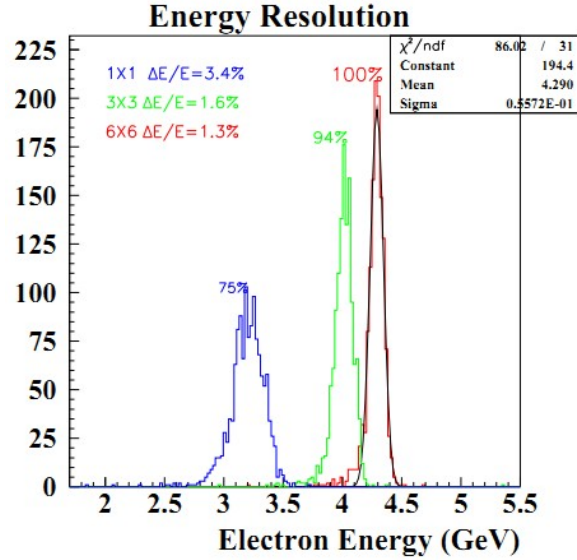


Figure 10: Energy response of a PbWO_4 crystal array to 4 GeV electrons. Left peak: single crystal; center peak: 3×3 array; right peak: 6×6 array.

5.4.2 Position resolution

The impact coordinates of the electrons incident on the crystal array were determined from the energy deposition of the electromagnetic shower in several neighboring counters. The distribution of the reconstructed coordinates for 4 GeV electrons hitting a crystal cell boundary is shown in Fig. 11. The linear dependence of the reconstructed coordinates obtained from a logarithmically weighted average of the cell signals *vs.* the impact positions determined by the scintillating fiber detectors is shown in Fig. 12. As is well known, there is a rather strong correlation between the position resolution ($\sigma_{x,y}$) and the point at which the incoming electrons hit the detector face. The top plot of the figure shows this dependence for the PbWO_4 crystals. The σ_x (1.28 mm) is smaller near the edge of the cell and increases to 2.1 mm at the cell center for 4 GeV electrons. Taking into account the 2 mm width of the scintillating fibers, the overall position resolution reached was $\sigma_{x,y} = 2.5 \text{ mm}/\sqrt{E}$.

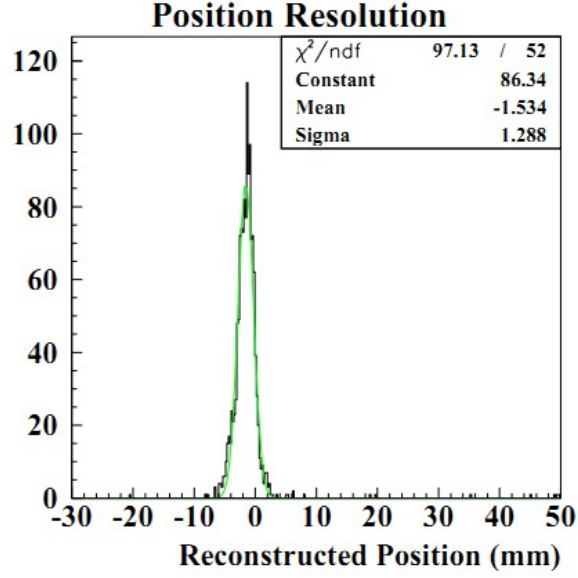


Figure 11: Distribution of reconstructed positions at the boundary between two PbWO_4 crystal detectors.

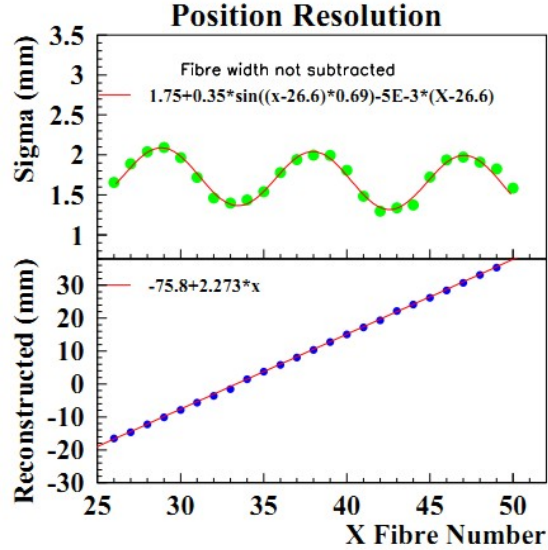
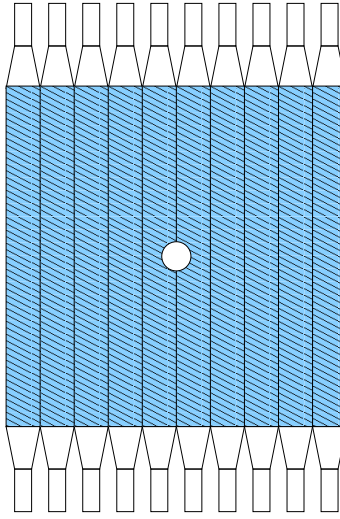


Figure 12: Position resolution (top) and reconstructed vs. actual position (bottom) of a PbWO_4 crystal array for 4 GeV electrons.

5.5 Veto counters

The veto counters are an $X - Y$ array of scintillator paddles in front of the calorimeter that will serve to veto neutral particle backgrounds. Ten scintillators in each direction with PMT on both ends will cover the full solid angle spanned by the calorimeter. A central hole ($4.1 \times 4.1 \text{ cm}^2$ in size) will be cut out in each plane for passage of the incident electron beam. In order to minimize photon conversion, only a single layer of 6.5 mm thick scintillator will be used for each plane. Time differences between signals from two ends of the scintillator will be used to determine the

position of the incident particles. Figure 13 shows a schematic of the X array of the veto counters, the Y array is similar.



X veto counter array with double PMTs

Figure 13: Schematic layout of the X veto counters array with PMTs on both ends and the central $4.1 \times 4.1 \text{ cm}^2$ hole for passage of the incident electron beam.

5.6 Electronics, data acquisition, and trigger

The proposed experiment will read out about 1230 channels of ADC and TDC information coming from three different detector systems. These include the PbWO_4 crystal calorimeter, the lead-glass preshower detector, and the $X - Y$ scintillator veto counters. The electronics will consist of FASTBUS, VME, CAMAC, and NIM standard crates. The digitization will be done entirely by FASTBUS LRS1877 TDC and LRS1881M ADC modules. Additionally, some VME scalars will read out and periodically inserted into the data stream. The triggering electronics will be done using NIM modules for fanning in calorimeter signals and discrimination.

The DAQ system for the proposed experiment is the standard JLab CODA based FASTBUS system utilizing the JLab designed Trigger Supervisor. A big advantage of the CODA/Trigger Supervisor system is the ability to run in fully buffered mode. In this mode, events are buffered in the digitization modules themselves allowing the modules to be “live” while being readout. This significantly decreases the deadtime of the experiment.

The trigger electronics is based on UVA120A (36 input, 2 output linear fan-ins) and UVA125A (quad 9 input linear fan-in with discriminator) NIM modules.

All electronics needed for the proton charge radius measurement DAQ and trigger, including the high voltage crates and all necessary cabling for the detectors, are available in Hall B from the PrimEx-II experiment.

Our approach in organizing the first level hardware trigger in this proposed experiment is to make it as simple as possible to reach the highest efficiency for the event selection process and in the mean time, to meet the DAQ rate requirements. The primary trigger will be formed from the PbWO_4 calorimeter by only using the analog sum of all dynode outputs from each of the crystal

cells. For fast summation of the analog signals, the UVA120 linear fan-in modules will be used as it was organized during the PrimEx-II experiment in Hall B.

The scattered electrons from the $ep \rightarrow ep$ reaction carry almost the same energy as the incident beam. Therefore, for this process alone, one can organize a very efficient trigger by requiring the total energy in the calorimeter to be $0.8 \times E_0$ including the resolutions. We are planning to detect simultaneously the electrons from the $e^-e^- \rightarrow e^-e^-$ process in this experiment in two single-arm and coincidence modes. For the coincidence mode, we are required to lower the total energy threshold level to about one-fifth of the beam energy – $0.2 \times E_0$ (see Fig. 16 including the resolutions. This will be still doable for this low luminosity ($\mathcal{L} \approx 6 \times 10^{28} \text{ cm}^{-2} \text{ s}^{-1}$) and low background experiment. The information from the other detectors (the veto counters) will be used during the off-line analysis of the experiment.

6 Experimental resolutions

6.1 Kinematics

Both $ep \rightarrow ep$ scattering and Møller scattering $e^-e^- \rightarrow e^-e^-$ are two-body reactions. Therefore, a minimum of two kinematical variables are required for the kinematical reconstruction of the reaction. For the selection of events from competing physics processes and accidental backgrounds, one needs to measure more than two variables in the experiment.

In this experiment the energy and momentum of the incident electron beam are known with high precision ($\Delta E/E \sim 10^{-4}$, emittance $\epsilon \sim 10^{-3}$ mm-mrad). In addition, for the $ep \rightarrow ep$ events, the energy and the (x, y) positions of the forward scattered electrons will be measured by the PbWO_4 calorimeter. The energy and momentum of the recoiling protons are very small (< 3 MeV) and will not be detected. Both scattered electrons from the Møller events will be detected in the calorimeter with measurement of the energies (E_1, E_2) and the (x, y) positions. Table 3 lists the incident beam energies and the Q^2 range for this experiment.

Table 3: Proposed kinematics for the proton charge radius measurement with the PbWO_4 calorimeter at 5 m from target.

E_{beam} (GeV)	θ_e (deg)	Q^2 (GeV/c) ²
1.1	0.7	$1.8 \cdot 10^{-4}$
	3.8	$5.2 \cdot 10^{-3}$
2.2	0.7	$7.2 \cdot 10^{-4}$
	3.8	$2.1 \cdot 10^{-2}$

6.1.1 $e - p$ scattering

Under the assumptions of one photon exchange the $e - p$ elastic scattering is described by the well known Rosenbluth formula [31]:

$$\frac{d\sigma}{d\Omega} = \left(\frac{d\sigma}{d\Omega} \right)_{\text{Mott}} \left(\frac{E'}{E} \right) \frac{1}{1 + \tau} \left(G_E^p{}^2(Q^2) + \frac{\tau}{\epsilon} G_M^p{}^2(Q^2) \right), \quad (21)$$

with

$$\begin{aligned} Q^2 &= 4EE' \sin^2 \frac{\theta}{2}, \\ \tau &= \frac{Q^2}{4M_p^2}, \\ \epsilon &= \left[1 + 2(1 + \tau) \tan^2 \frac{\theta}{2} \right]^{-1}, \\ E' &= \frac{E}{1 + \frac{2E}{M_p} \sin^2 \frac{\theta}{2}}, \end{aligned}$$

where Q^2 is the four-momentum transfer squared, $G_E^p(Q^2)$ and $G_M^p(Q^2)$ are the protons electric and magnetic form factors, ϵ is the virtual photon longitudinal polarization parameter, E and E' the incident and scattered electron energies, θ the laboratory scattering angle of the electron and M_p the proton mass.

Figures 14 and 15 show the range of the scattered electron's energy and four-momentum transfer squared as a function of the laboratory scattering angle.

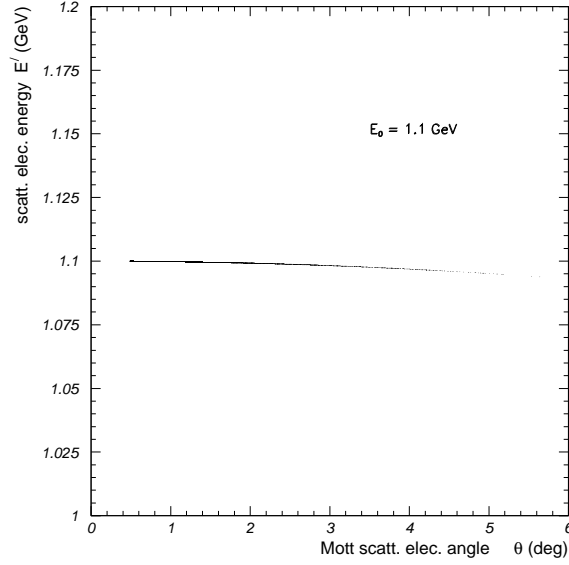


Figure 14: Energy of the scattered electron in $e - p$ scattering vs. the laboratory scattering angle at an incident beam energy of 1.1 GeV.

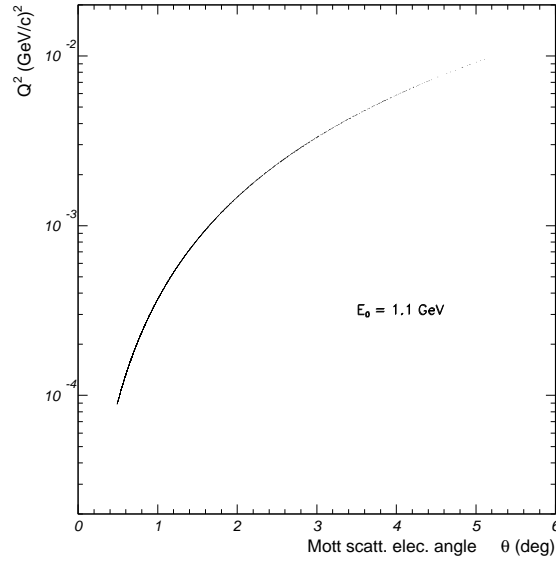


Figure 15: Q^2 of the scattered electron in $e - p$ scattering vs. the laboratory scattering angle at an incident beam energy of 1.1 GeV.

6.1.2 Møller scattering

The Møller $e^-e^- \rightarrow e^-e^-$ differential cross section, at tree level, is getting contributions from the s and t photon exchange channels. In the center-of-mass (CM) system it is given by

$$\frac{d\sigma}{d\Omega} = \frac{\alpha^2}{s} \frac{(3 + \cos^2 \theta^*)^2}{\sin^4 \theta^*} \quad (22)$$

for high energies where the electron mass m_e can be neglected. Here $\alpha = 1/137$ is the fine structure constant, θ^* is the CM system polar scattering angle, and s is the interaction energy squared.

Some obvious features of the Møller scattering can be deduced from Eq. 22.

- The cross section is seen to diverge at $\cos \theta^* = \pm 1$. This is due to the fact that the electron mass was neglected. In a rigorous treatment, where m_e is not neglected, the Møller scattering formula remains finite even at $\cos \theta^* = \pm 1$.
- The magnitude of the cross section decreases as s increases, similar to that of the e^+e^- annihilation process.

In the scattering of two electrons, s may be written in a Lorentz invariant form as

$$s = 2m_e^2 + 2m_e E_B, \quad (23)$$

where E_B is the beam energy.

The laboratory momentum of the scattered electron, p_{lab} is given by

$$p_{\text{lab}} = \gamma_{\text{CM}} \sqrt{(E^* + p^* \beta_{\text{CM}} \cos \theta^*)^2 - \frac{m_e^2}{\gamma_{\text{CM}}^2}}, \quad (24)$$

where p^* , E^* are the momentum and energy of the incident electron in the CM system and γ_{CM} is the Lorentz factor. The relation between the laboratory scattering angle θ_{lab} and the CM scattering angle θ^* is given by

$$\tan \theta_{\text{lab}} = \frac{1}{\gamma_{\text{CM}}} \cdot \frac{\sin \theta^*}{\beta_{\text{CM}}/\beta^* + \cos \theta^*}, \quad (25)$$

where β_{CM} is the velocity of the CM system and β^* is the velocity of the electron in the CM system.

In the CM system of the Møller scattering, the momentum and energy of the incident electron are expressed by:

$$\begin{aligned} p^* &= \sqrt{\frac{m_e(E_B - m_e)}{2}} \quad \text{and} \\ E^* &= \sqrt{\frac{m_e(E_B + m_e)}{2}}. \end{aligned} \quad (26)$$

From Eqs. 23-26 it follows that

$$p_{\text{lab}} = \frac{p_B}{2} (1 + \cos \theta^*) \quad (27)$$

so that the laboratory momentum of the scattered electron does not depend on the CM total energy, but only on the beam energy and the CM scattering angle. From Eq. 25 one obtains the expression:

$$\tan^2 \theta_{\text{lab}} = \frac{2m_e}{E_B + m_e} \cdot \frac{1 - \cos \theta^*}{1 + \cos \theta^*}. \quad (28)$$

The minimum opening angle in the laboratory system between the two electrons in the Møller scattering is when $\theta^* = \pi/2$:

$$\tan^2 \theta_{\text{lab}} = \frac{2m_e}{E_B + m_e} . \quad (29)$$

Figure 16 shows one of the Møller scattered electrons' energy vs. its angle. The angular correlation between the two scattered electrons in the laboratory system is shown in Fig. 17 and the opening angle as a function of beam energy in Fig. 18. The kinematical distribution of the $X - Y$ positions of the two Møller electrons is shown in Fig. 6.

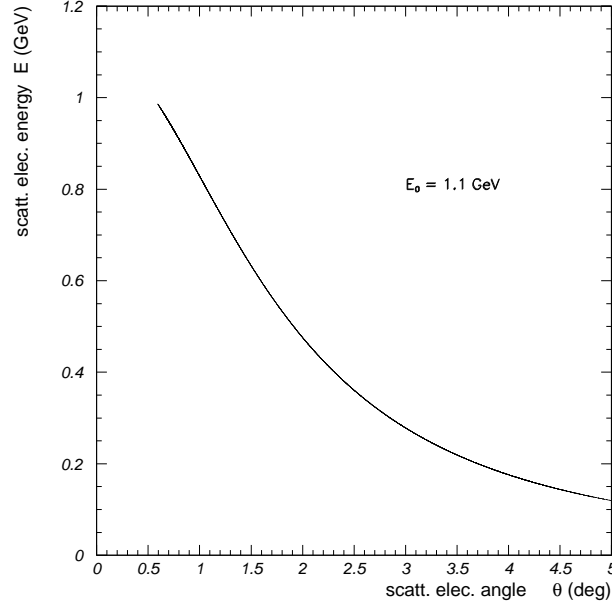


Figure 16: Energy of one of the electrons in Møller scattering vs. the laboratory scattering angle at an incident beam energy of 1.1 GeV.

6.2 Resolutions

In this experiment, the scattered electrons from $e - p$ elastic and Møller scatterings will be detected with a high resolution and high efficiency PbWO_4 electromagnetic calorimeter. The energy and positions of the scattered electrons will be measured with high resolution:

$$\begin{aligned} \sigma_E/E &= 2.6\%/\sqrt{E} , \\ \sigma_{x,y} &= 2.5 \text{ mm}/\sqrt{E} . \end{aligned}$$

(Details of energy and position resolutions are given in Secs. 5.4.1 and 5.4.2.)

Detailed Monte Carlo simulations for $e - p$ elastic and Møller scatterings were carried out in order to study the the energy and position resolutions of detecting the scattered electrons over the full acceptance of the calorimeter.

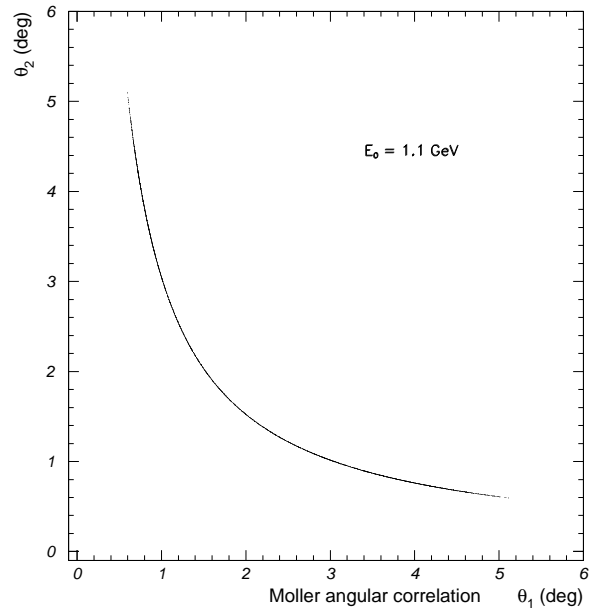


Figure 17: Angular correlation of the two electrons in Møller scattering in the laboratory system at an incident beam energy of 1.1 GeV.

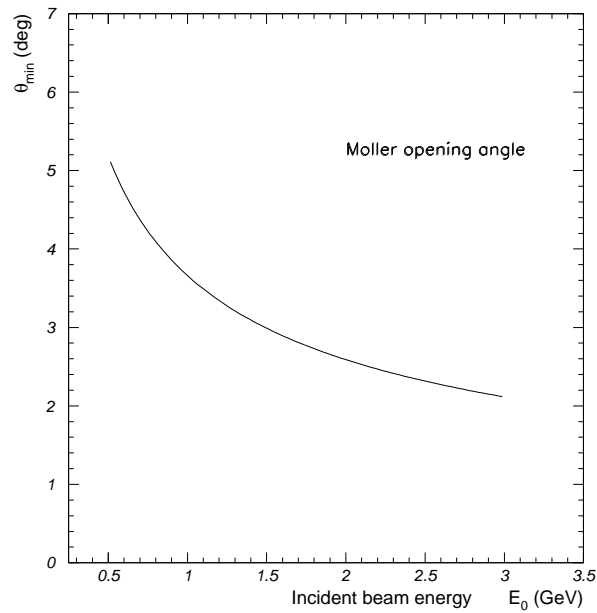


Figure 18: The minimum opening angle in the laboratory system of the two electrons in Møller scattering as a function of incident beam energy.

6.2.1 $e - p$ scattering

Figure 19 shows the “elasticity”, $(E_0 - E')$, distribution of the electrons in $e - p$ elastic scattering. An excellent energy resolution of $\sigma_E = 27$ MeV is seen at $E_0 = 1.1$ GeV. The corresponding distribution of polar angular resolution is shown in Fig. 20, $\sigma_{\theta_e} = 0.5$ mrad is expected in this experiment. The polar angular range implemented in generating these distributions is $\theta_e \geq 0.7^\circ$.

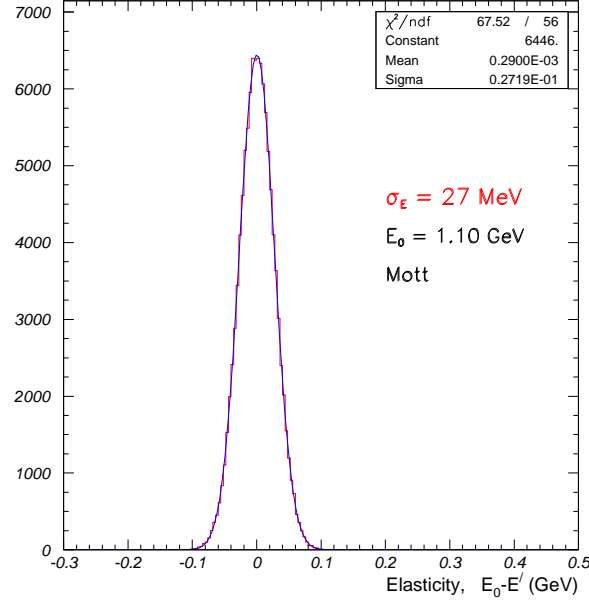


Figure 19: The “elasticity”, $(E_0 - E')$, distribution of detecting the electrons in $e - p$ elastic scattering at $E_0 = 1.1$ GeV. The minimum scattering angle cut implemented is $\theta_e \geq 0.7^\circ$.

One of the key considerations in this precision measurement is the Q^2 resolution that is expected in this experiment. Figure 21 shows the Q^2 resolutions at the minimum and maximum scattering angles of the calorimeter acceptance at a distance of 5 m with $E_0 = 1.1$ GeV.

6.2.2 Møller scattering

The elasticity, $(E_0 - (E_1 + E_2))$, distribution of the Møller scattered electrons is shown in Fig. 22 for 1.1 GeV incident beam energy.

An important criterion that needs to be satisfied for the two electrons in Møller scattering is that they have to be co-planar in the azimuthal direction, $\varphi_{e1} - \varphi_{e2} = \pi$. Figure 23 shows the resolution of the co-planarity requirement at $E_0 = 1.1$ GeV.

A clear identification of the $e - p$ elastic scattering electrons from the Møller electrons requires that the tails of their energy distribution do not have any significant overlap. This condition can be achieved by requiring that the polar scattering angles of the electrons are above a certain minimum value. Figure 24 shows that above $\theta_e = 0.7^\circ$ the electrons from the two processes can be cleanly separated for $E_0 = 1.1$ GeV. A similar plot for $E_0 = 2.2$ GeV is shown in Fig. 25. Here, the ep elastic scattered electrons are separated from the Møller scattered electrons without the need for an angular cut; the events with $\theta_e < 0.4^\circ$ are not in the acceptance region of the calorimeter.

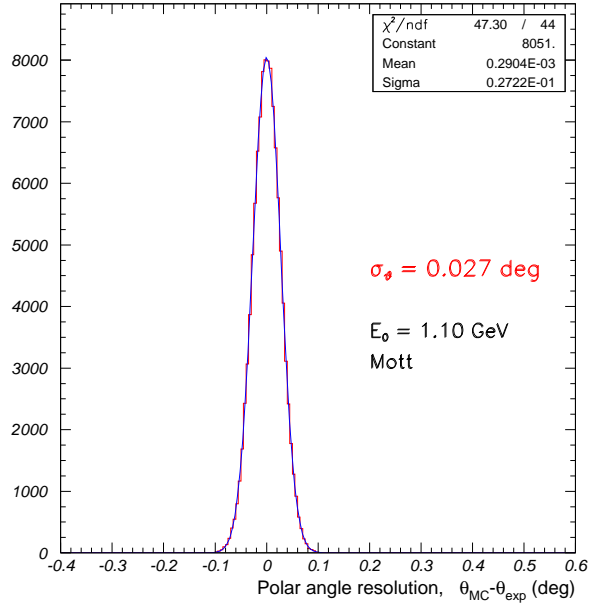


Figure 20: The polar angle resolution of detecting the electrons in $e - p$ elastic scattering at $E_0 = 1.1 \text{ GeV}$. The minimum scattering angle cut implemented is $\theta_e \geq 0.7^\circ$.

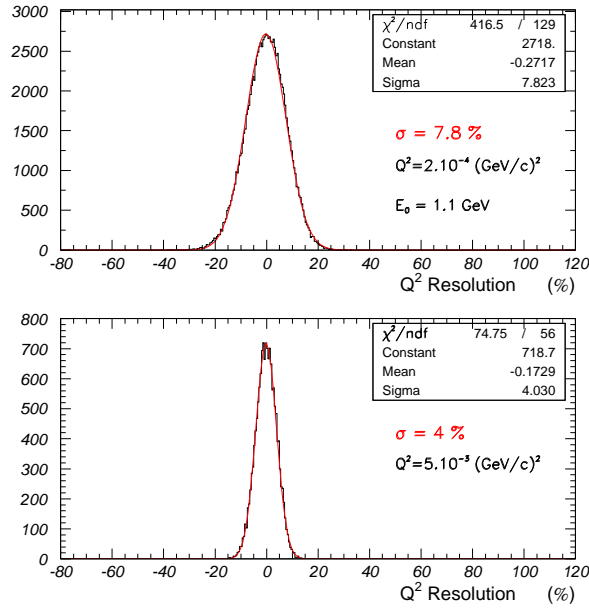


Figure 21: The Q^2 resolution of detecting the electrons in $e - p$ elastic scattering at $E_0 = 1.1 \text{ GeV}$. The top plot is for $\theta_{\min} = 0.7^\circ$ and the bottom plot is for $\theta_{\max} = 3.8^\circ$. The PbWO_4 calorimeter is placed at a distance of 5 m from the target.

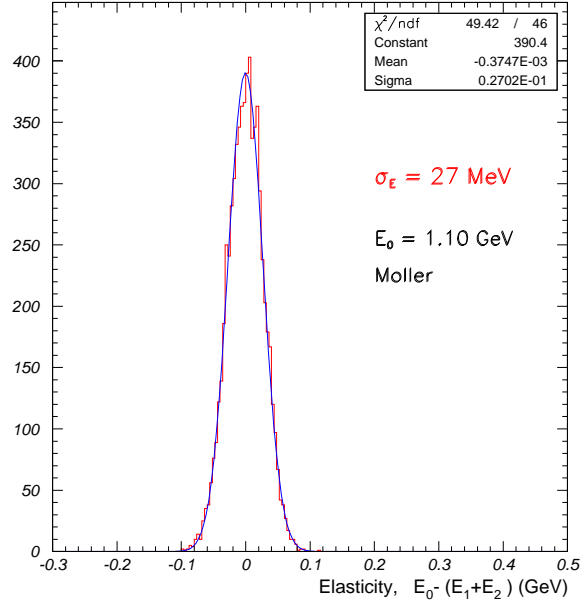


Figure 22: The “elasticity”, $E_0 - (E_1 + E_2)$, distribution of detecting the electrons in Møller scattering at $E_0 = 1.1 \text{ GeV}$. The minimum scattering angle cut implemented is $\theta_e \geq 0.7^\circ$.

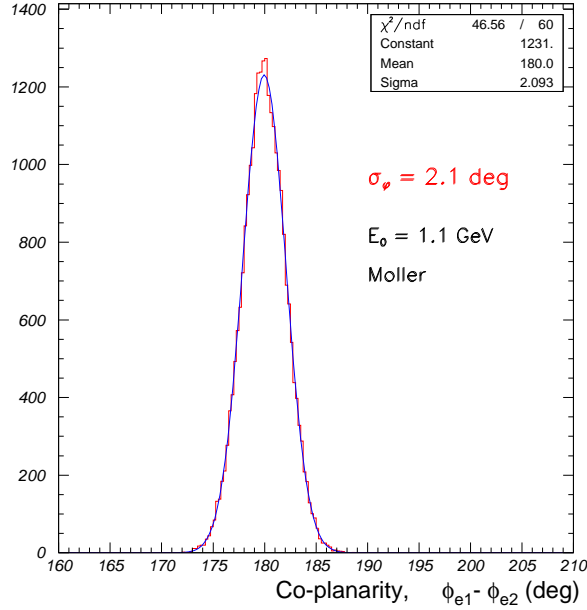


Figure 23: The coplanarity distribution in the azimuthal direction, $\varphi_{e1} - \varphi_{e2}$, of the two electrons in Møller scattering at $E_0 = 1.1 \text{ GeV}$. The minimum scattering angle cut implemented is $\theta_e \geq 0.7^\circ$.

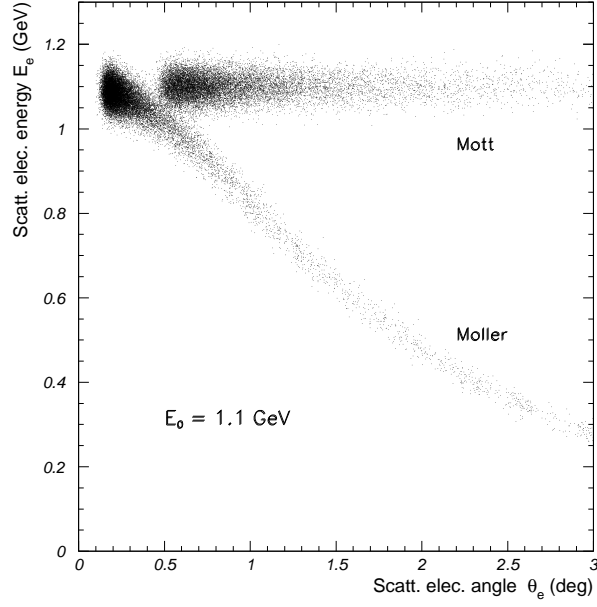


Figure 24: The energy vs. scattering angle distribution of $e - p$ elastic and Møller scattered electrons at $E_0 = 1.1$ GeV. A minimum scattering angle cut of $\theta_e = 0.7^\circ$ is required to clearly identify the electrons from the two processes.

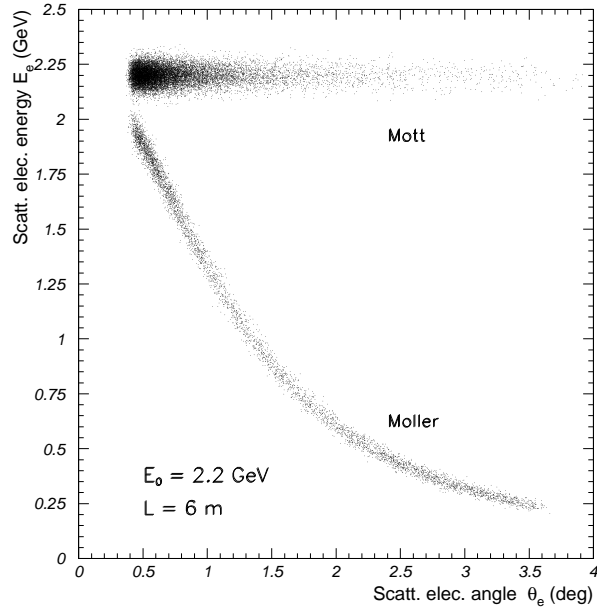


Figure 25: The energy vs. scattering angle distribution of $e - p$ elastic and Møller scattered electrons at $E_0 = 2.2$ GeV. No minimum scattering angle cut on θ_e is required here to clearly identify the electrons from the two processes.

7 Radiative corrections at forward angles

The radiative corrections to the unpolarized elastic ep scattering cross sections were determined by two methods. The first one used the calculation of Maximon and Tjon [77]. Only the leptonic model independent terms were considered. The second one used the MASCARAD code [78]. Both methods, with appropriate kinematical cuts, give similar results within 3% up to $Q^2 = 10^{-4}$ GeV^2 . At $E_{beam} = 1.1$ GeV and for $1.8 \cdot 10^{-4} \text{ GeV}^2 \leq Q^2 \leq 5.2 \cdot 10^{-3} \text{ GeV}^2$ a correction δ to the unpolarized cross sections of $9\% \leq \delta \leq 15\%$ was found. At $E_{beam} = 2.2$ GeV and for $7.2 \cdot 10^{-4} \text{ GeV}^2 \leq Q^2 \leq 2.1 \cdot 10^{-2} \text{ GeV}^2$, $11\% \leq \delta \leq 18\%$. The effect of radiative corrections is known to better than 0.5%. It is important to point out that for very low Q^2 ($\sim 10^{-5}$) MASCARAD presents some instabilities whereas the results obtained with the Maximon and Tjon calculation remain stable. This instability comes from the part that is subtracted from the real photon emission in order to cancel the infrared divergence. Large and negative contributions can be obtained but must cancel with the respective factorized correction. However, this correction is calculated using the approximation $m_e^2 \ll Q^2$ whereas the integration for the real photon emission is carried out without it. As consequence, this can be a source of instability in the very low Q^2 region. As for the Maximon and Tjon calculation, both $m_e^2 \ll Q^2$ and soft photon approximations are used, leading a result less sensitive to instabilities at very low Q^2 . The quality of the soft photon approximation is difficult to control without exact calculation of RC in the style of MASCARAD, therefore, in order to obtain a precise estimation of the radiative correction at very low Q^2 one needs to have a full calculation beyond both the $m_e^2 \ll Q^2$ approximation and the soft photon approximation in elastic ep scattering. One expert in radiative corrections among the collaboration plans to develop and carry out such calculation. Experimentally, it would also be possible to reduce the hard photon contribution since we will be able to detect the hard photon in the calorimeter.

A Monte Carlo simulation was written to study the effect of the detectors resolutions on the Q^2 determination. Since two-body elastic kinematics is over determined, only angles were generated randomly following a uniform distribution between 0.7 and 3.8 degrees and the scattered energy was determined by the kinematics. Both distributions were then smeared by a Gaussian of width equal to detector resolutions: $\sigma_{E'} = 2.6\%/\sqrt{E}$ with E in GeV and $\sigma_\theta = 0.35$ mrad. The radiative tail in the E' spectrum is simulated with a Landau distribution. The scattered electron energy and Q^2 distributions are shown in Figs. 26 and 27 respectively.

The generated data are then binned in small bins of E' and θ . For each bin the mean $Q_{smeared}^2$ is calculated and it is compared to $Q_{nom.}^2$ obtained without any resolution effect. One defines a correction factor for each bin as $r = (Q_{nom.}^2 - Q_{smeared}^2)/Q_{nom.}^2$, which will be used to correct the value of Q^2 in each bin. This simple simulation shows an average value over all (E', θ) bins of 24% for r for both beam energies. Such a change in Q^2 will induce a variation strictly below 1% of the radiative correction to the elastic ep unpolarized cross sections. A full Monte Carlo simulation, with a more refined radiative correction implementation following the latest development [79] is in progress. Its results will be reported prior to the defense of the proposal. The radiative corrections to the Møller are well known [80] and their calculation and implementation in the full simulation is also in progress.

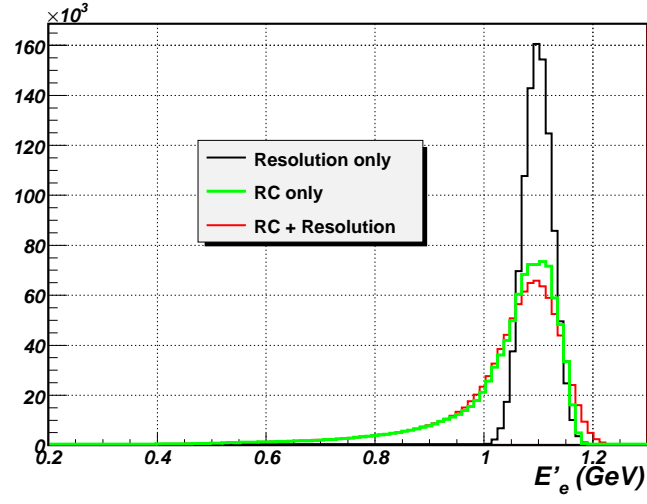


Figure 26: Simulated scattered electron energy. In black with only the resolution contributions, in green with only radiative corrections and in red with both contributions.

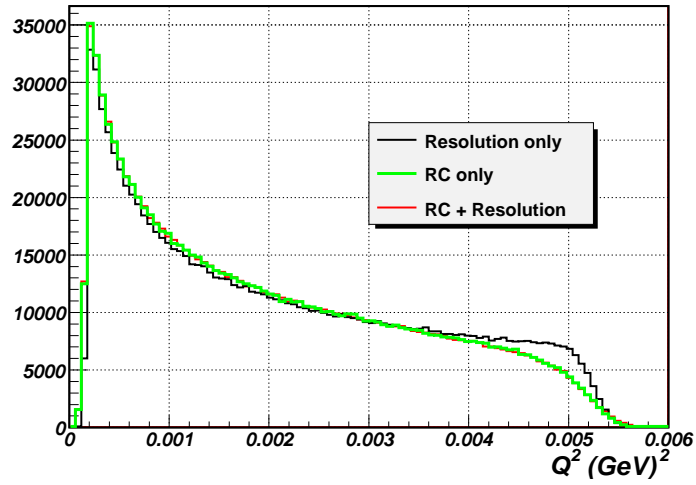


Figure 27: Simulated scattered electron energy. In black with only the resolution contributions, in green with only radiative corrections and in red with both contributions.

8 Extraction of proton charge radius

As described in Sec. 4, the ep elastic cross sections in this proposed experiment will be measured by normalizing to the Møller cross sections. The Møller cross sections will be obtained from theoretical QED calculations within particular acceptances (see Fig. 3), taking into account the radiative effects. At this Q^2 range, the contribution from $G_M^p(Q^2)$ in Eq. 4 is negligible within the accuracy of this experiment. Then the electric form factor, G_E^p , can be extracted from the measured ep elastic cross sections vs. Q^2 . The slope of G_E^p vs. Q^2 at this very low Q^2 range will determine the rms proton charge radius, r_p (see Eq. 7).

In order to investigate the uncertainties in the extraction of r_p , a full Monte Carlo simulation code based on GEANT3.21 package has been developed which takes into account the realistic geometry of the experimental setup, including all resolutions of the detector. This program generates events based on theoretical cross sections which are then traced through the target and detection system. The Monte Carlo generated events are then analyzed to reconstruct the “measured” differential cross sections. In this scheme one can obtain the uncertainties in r_p vs. detector resolutions, geometrical acceptances, misalignments of beam and experimental setup. This program takes in account the radiative processes inside of the hydrogen gas target. However, the so called “internal” or the soft radiative effects are not yet included in this code. We are in the process of implementing the full radiative effects in this code in order to get effects of their corrections in the extracted proton charge radius. One important advantage of the calorimetric method over the traditional magnetic spectrometer method is that in this case we have a parallel measurement of the part of the radiative effects, related to target bremsstrahlung, the so called hard radiative effects. This fact, together with the extremely low contributions from the hydrogen gas target, will significantly reduce the effects of radiative corrections in this proposed experiment. The results from the fully implemented corrections in the Monte Carlo code will be reported prior to the defense of the proposal.

Four examples of these preliminary simulations are illustrated in Figs. 28, 29, 30 and 31 for part of the statistics for the incident beam energies $E_0 = 1.1$ GeV and $E_0 = 2.2$ GeV. In Figs. 28 and 30, in the event generator the value of $r_p = 0.8768$ fm was set, while in Figs. 29 and 31 it is $r_p = 0.8418$ fm. As demonstrated in these preliminary studies, the measured G_E^p at this Q^2 range has a good sensitivity from r_p to reach the sub-percent level of extraction.

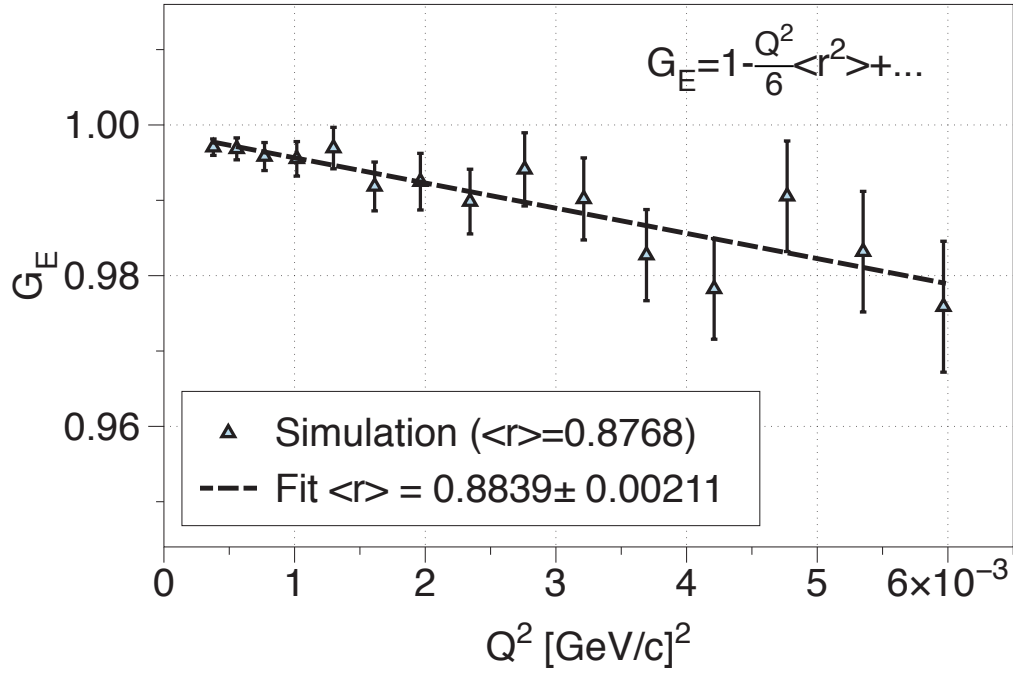


Figure 28: Extraction of G_E^p from Monte Carlo generated data set for $E_0 = 1.1$ GeV for the value of $r_p = 0.8768$ fm. The error bars shown are statistical only.

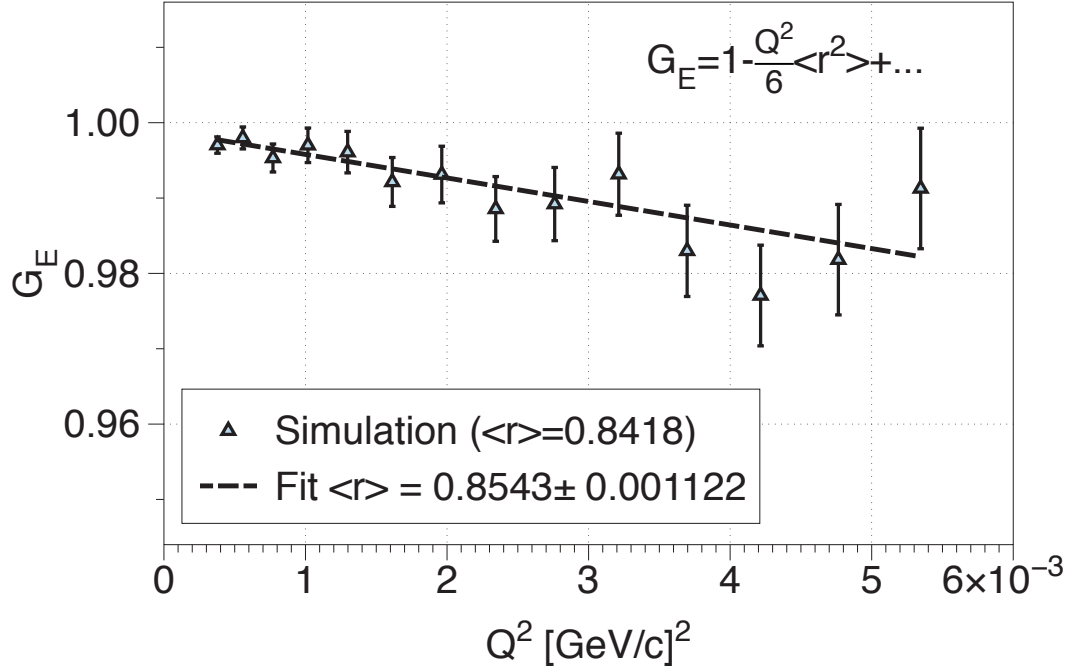


Figure 29: Extraction of G_E^p from Monte Carlo generated data set for $E_0 = 1.1$ GeV for the value of $r_p = 0.8418$ fm. The error bars shown are statistical only.

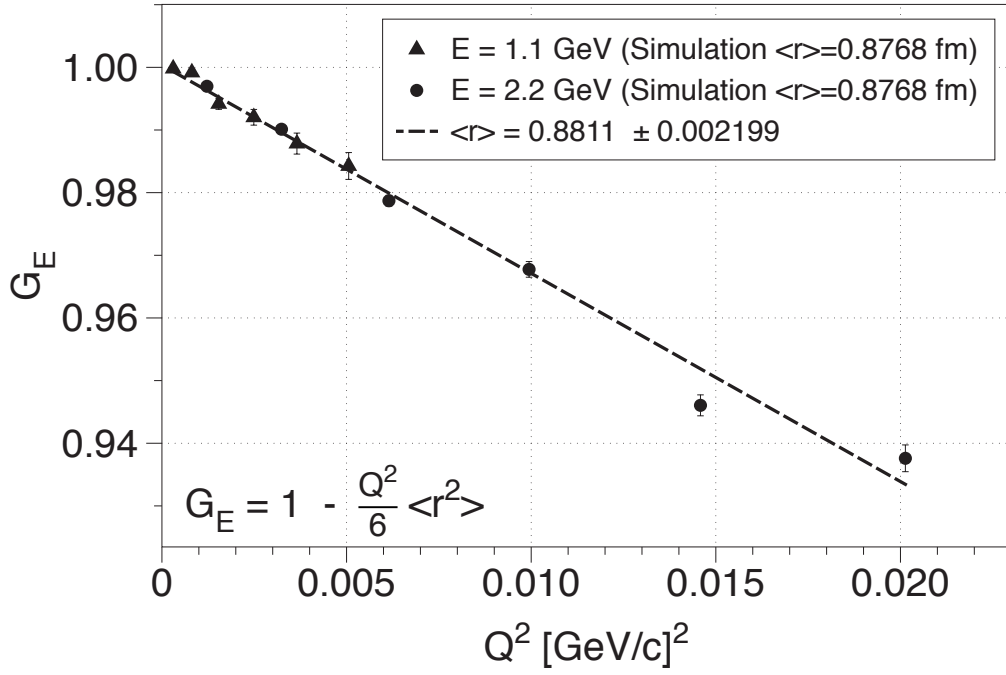


Figure 30: Extraction of G_E^p from Monte Carlo generated data set for $E_0 = 1.1$ GeV and $E_0 = 2.2$ GeV runs for the value of $r_p = 0.8768$ fm. The error bars shown are statistical only.

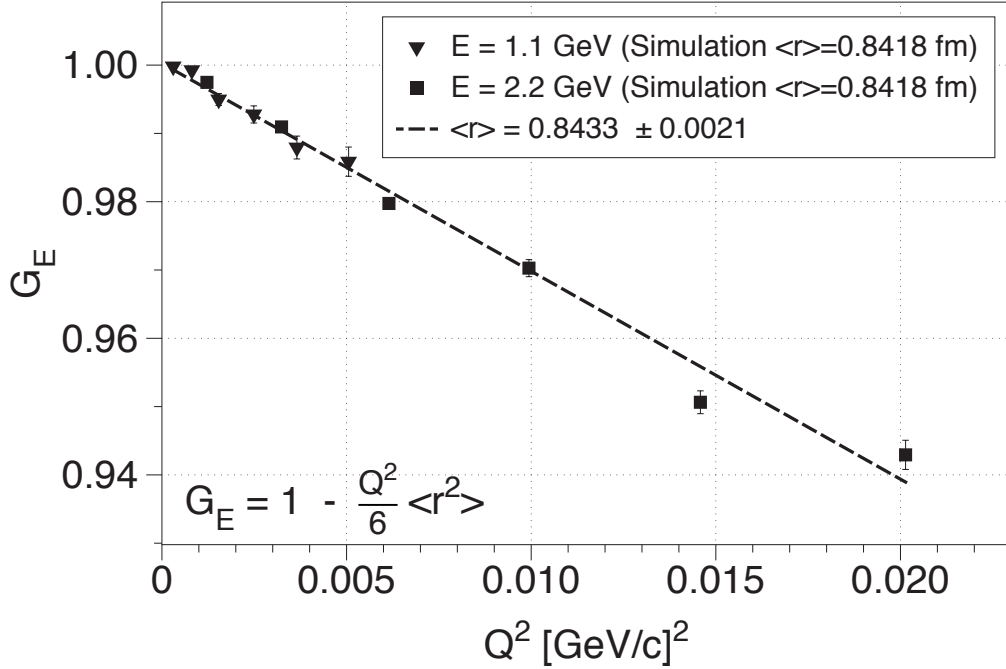


Figure 31: Extraction of G_E^p from Monte Carlo generated data set for $E_0 = 1.1$ GeV and $E_0 = 2.2$ GeV run for the value of $r_p = 0.8418$ fm. The error bars shown are statistical only.

9 Statistics, event rate and beam time

For the statistics and event rate estimation, a full Monte Carlo program was developed based on GEANT3.21 package. This program samples both $ep \rightarrow ep$ and $e^-e^- \rightarrow e^-e^-$ processes according to their differential cross sections and traces the events through the target and detector setup. The energies and positions of the secondary particles were sampled in the calorimeter according to their experimental resolutions described in Secs. 5.4.1 and 5.4.2.

The hydrogen gas target in this experiment is projected to have $N_{\text{tgt}} = 1 \cdot 10^{18}$ H atoms/cm². In that case, with the incident electron beam intensity of $I_{\text{beam}} = 10$ nA ($N_e = 6.25 \cdot 10^{10}$ e⁻/s) the rate for the $ep \rightarrow ep$ scattered elastic electrons on the PbWO₄ calorimeter will be:

$$N_e^{\text{RB}} = N_e \cdot N_{\text{tgt}} \cdot \Delta\sigma \cdot \varepsilon_{\text{geom}} \cdot \varepsilon_{\text{det}} ,$$

where $\Delta\sigma$ is the integrated Rosenbluth (RB) cross section at forward angles ($\theta_e = 0.15^\circ - 10^\circ$); $\Delta\sigma \cdot \varepsilon_{\text{geom}}$ is part of the integrated cross section accepted by our setup. For these calculations, we assume that the detection efficiency $\varepsilon_{\text{det}} \approx 1$. With all that, the rate of electrons from the $ep \rightarrow ep$ process is

$$\begin{aligned} N_e^{\text{RB}} &= 6.25 \cdot 10^{10} \cdot 1 \cdot 10^{18} \cdot 3.14 \cdot 10^{-26} \cdot 0.0754 \text{ e}^-/\text{s} \\ &\simeq 150 \text{ e}^-/\text{s} \\ &\simeq 12.8\text{M e}^-/\text{day} . \end{aligned}$$

This is a high integrated statistics per day for the forward angles. However, due to $\sim 1/\sin^4(\theta/2)$ nature of the scattering process, most of these events are populated in the extreme forward angles ($\theta_e \sim 0.5^\circ$ for our acceptance range). Therefore, in order to provide $\leq 0.5\%$ statistical uncertainty also for the last Q^2 bin ($\theta_e = 3.55^\circ - 3.77^\circ$), we are required to run 2 days for this $E_0 = 1.1$ GeV energy setting:

$$\begin{aligned} N_e^{\text{RB}}(Q^2=4.9 \pm 0.3 \cdot 10^{-3}) &= 6.25 \cdot 10^{10} \cdot 1 \cdot 10^{18} \cdot 3.14 \cdot 10^{-26} \cdot 1.7 \cdot 10^{-4} \text{ e}^-/\text{s} \\ &\simeq 0.334 \text{ e}^-/\text{s} \\ &\simeq 57,600 \text{ e}^-/2 \text{ days} . \end{aligned}$$

The $e^-e^- \rightarrow e^-e^-$ Møller cross section is significantly higher than the $ep \rightarrow ep$ cross section for the same incident beam intensity and target thickness:

$$\begin{aligned} N_{e^-e^-}(\text{coin.}) &= 6.25 \cdot 10^{10} \cdot 1 \cdot 10^{18} \cdot 0.68 \cdot 10^{-24} \cdot 0.0048 \text{ e}^-e^-/\text{s} \\ &\simeq 200 \text{ e}^-e^-/\text{s} \\ &\simeq 17.3\text{M e}^-e^-/\text{day} . \end{aligned}$$

In order to address the rate of hadronic (π^+) contribution in this experiment, detailed calculations were performed using the EPC/Wiser/SAID codes. Table 4 shows the rate for π^+ production and ep elastics for forward angles at $E_0 = 1.1$ GeV and 2.2 GeV. As expected for these forward angles, the estimated π^+/e ratio is less than $\sim 10^{-3}$. With this low hadronic rate, the PbWO₄ electromagnetic calorimeter itself with its π/e rejection capability of $\sim 10^{-2}$ will cut down the hadronic background.

Table 4: Rates of π^+ , proton, π^0 , and ep elastics for forward angles at two different energies.

θ (deg)	$E_0 = 1.1 \text{ GeV}$				$E_0 = 2.2 \text{ GeV}$			
	π^+ (Hz)	p (Hz)	π^0 (Hz)	ep (Hz)	π^+ (Hz)	p (Hz)	π^0 (Hz)	ep (Hz)
0.5	$1.4 \cdot 10^{-4}$	$1.0 \cdot 10^{-5}$	$5.0 \cdot 10^{-5}$	$2.3 \cdot 10^3$	$2.4 \cdot 10^{-4}$	$5.2 \cdot 10^{-5}$	$2.4 \cdot 10^{-4}$	56
1.0	$1.1 \cdot 10^{-3}$	$7.7 \cdot 10^{-5}$	$5.5 \cdot 10^{-4}$	106	$1.8 \cdot 10^{-3}$	$5.3 \cdot 10^{-4}$	$2.5 \cdot 10^{-3}$	26
2.0	$2.2 \cdot 10^{-3}$	$1.6 \cdot 10^{-4}$	$1.2 \cdot 10^{-3}$	13.7	$3.8 \cdot 10^{-3}$	$1.1 \cdot 10^{-3}$	$5.2 \cdot 10^{-3}$	3.4
3.0	$3.5 \cdot 10^{-3}$	$2.5 \cdot 10^{-4}$	$1.8 \cdot 10^{-3}$	4.2	$6.0 \cdot 10^{-3}$	$1.7 \cdot 10^{-3}$	$8.9 \cdot 10^{-3}$	1.0

In summary, with $I_{\text{beam}} = 10 \text{ nA}$ and $N_{\text{tgt}} = 1 \cdot 10^{18} \text{ H atoms/cm}^2$, two days of run time will be sufficient to get the required high statistics for all Q^2 points including the very last one, $Q^2 = 4.9 \pm 0.3 \cdot 10^{-3} (\text{GeV/c})^2$.

We also request to have a separate run with $E_0 = 2.2 \text{ GeV}$ to increase the Q^2 range for a more stable fit of the G_E^p vs. Q^2 to extract the proton charge radius. The Møller cross section is inversely proportional to the beam energy, so we will have twice less cross section. On the other hand, the geometrical acceptance of the $e^-e^- \rightarrow e^-e^-$ reaction increases with the energy also. With all that, the Møller rate at $E_0 = 2.2 \text{ GeV}$ will be of the same order as for the first energy. For the $ep \rightarrow ep$ elastic scattering process the cross section drops as $1/E^2$ and, therefore, all rates for the 2.2 GeV run will be four times less than for those at 1.1 GeV. However, we request two days of run for this energy also. This will provide sufficient statistics for most part of the Q^2 range, except for the few points at larger Q^2 where we will have statistical uncertainties still less than 1%.

With this, we are requesting two days of run time for each of the energy settings to have sufficient statistics for the precision extraction of the proton charge radius. We will need 3.5 more days for setup checkout, tests and calibration, and 5 days for commissioning the new gas flow target. The energy change from one-pass to two-pass will require about half-a-day.

In order to control the experimental background originating from the electron beam halo (beam signal peak/halo ratio is $\sim 10^7 - 10^8$) hitting the cell wall of the gas flow target, we will need a total of 2 days of empty target runs. These runs will be performed periodically during the entire time of the experiment. With that, we are requesting a total of 15 days to perform this experiment and extract the proton charge radius with a sub-percent precision.

Table 5: Beam time request.

	Time (days)
Setup checkout, tests and calibration	3.5
Gas target commissioning	5
Statistics at 1.1 GeV	2
Energy change	0.5
Statistics at 2.2 GeV	2
Empty target runs	2
Total	15

10 Estimated uncertainties

The cross sections for the two processes, ep and e^-e^- Møller, which we are aiming to measure simultaneously in this proposed experiment, are the most highest two electromagnetic processes at these forward angles. Based on the rates estimated in Sec. 9, we expect to have enough statistics within the requested beam time, to provide statistical uncertainties on the level of 0.2% for each Q^2 point. For the lower Q^2 points, this number would be significantly less than 0.2%. With that, the major concern for this type of experiments, for sure, is the control of the systematic uncertainties, and estimation of them in the final uncertainty of the extracted proton charge radius. We are convinced that the proposed experiment with its: (1) possibility to reach very low Q^2 range; (2) with normalizing the ep cross sections to a well known QED process, like the Møller scattering; and (3) very low density windowless hydrogen gas target to minimize the physics background processes, is currently the most optimized ep measurement to extract the proton charge radius with a sub-percent precision.

The main sources of systematic uncertainties in this proposed experiment from the experimental setup are:

- (1) misalignment in position reconstruction;
- (2) misalignment of beam position and angle on the PbWO_4 calorimeter;
- (3) calorimeter energy miscalibration.

The energy calibration of the calorimeter will be performed by the Hall B photon tagger at $E_0 = 1.1$ and 2.2 GeV. The energy accuracy of the tagger is at the level of $\sim 10^{-3}$. Therefore, its contribution to the uncertainty in Q^2 will be at the same level.

The uncertainty in position of the calorimeter on the beam line will be performed by engineering survey with an accuracy of ~ 0.7 mm. In addition, the coplanarity of the $e^-e^- \rightarrow e^-e^-$ process will be used in offline analysis to obtain a finer definition of the electron beam's position and angle on the calorimeter.

As it is described in Sec. 4, the ep cross sections will be measured with respect to the Møller. Therefore, the two major systematic uncertainties, most typical for other ep experiments, will directly cancel out in the ratio. The remaining systematic uncertainties will depend on the method with which we identify the Møller events and, therefore, the cross sections for that particular Q^2 bin. The single-arm method, described in Sec. 4.2.1, is the best way to further cut down the sources of the systematic uncertainties in the simulation of the Møller cross section for a particular Q^2 bin since it will be calculated in the same ep acceptance. Implementation of this method depends only on the level of the radiative tails on the ep scattered electrons. We are in the process of performing full simulations of these type of effects, the results will be submitted prior to the defense of the proposal.

With the single-arm Møller event selection method, the estimated uncertainty on the Møller cross section calculation is on the level of 0.4%, including the electromagnetic corrections. Combining that with the 0.2% statistical uncertainty, we estimate the total uncertainty on the r_p extraction to be on the level of 0.45%.

For the two other Møller event selection methods, two more items are remaining in the determination of the ep cross sections, the partially different geometrical acceptances and detection

efficiencies. The differences of the detection efficiencies for the different part of the detection system, based on our previous experiences, is expected to be rather small. Therefore, that part will not contribute significantly in the final uncertainty. For the “two-ring” acceptance determinations (see Secs. 4.2.2 and 4.2.3), the estimated uncertainty should not exceed the 0.3% level. With that, for the second and third methods the total uncertainty is estimated to be 0.55%, including the 0.2% statistical uncertainty and it is shown in Table 6.

Table 6: Total estimated uncertainty for the second and third Møller events identification methods.

Item	Uncertainty (%)
Statistical uncertainty	0.2
Ratio in detection efficiency	<0.1
Ratio in acceptance (including Q^2 determination)	0.4
Radiative corrections	0.3
Fitting procedure	0.2
Hadron rejection	<0.1
Neutral rejection	<0.1
Total	0.6

11 Summary

The proton charge radius is one of the fundamental quantities in physics. Precision knowledge of its value is critically important for the understanding of the structure of nucleon in terms of quark and gluon degrees of freedom in the theory of strong interactions – QCD. On the other hand, the precise determination of the charge radius is very important for atomic physics to test calculations of bound-state QED and, in particular, spectroscopy of atomic hydrogen.

There are three major methods to measure the proton charge radius. The ep elastic scattering method, in which the slope of the extracted electric form factor, G_E^p , at low Q^2 defines the rms radius of the proton. For this type of experiments, typical uncertainties obtained is at the level of 2%. The average value of the charge radius for this method, given by a model independent analysis of electron scattering data is $r_p = 0.871(10)$ fm.

Another method uses the spectroscopy of electronic hydrogen atom through the Lamb shift measurements. The value of the charge radius from this method is consistent with the ep scattering results: $r_p = 0.8768(69)$ fm.

Very recently, in 2010, results from two more precision measurements of the charge radius have been published. The first one is from new studies of muonic hydrogen performed at PSI providing a factor of ten more precise result than all previous experiments: $r_p = 0.84184(67)$ fm. The second result is from Mainz done with the traditional ep method giving $r_p = 0.879(8)$ fm and it is consistent with previous ep results. The muonic hydrogen result is five standard deviations smaller than the CODATA average. This experimental fact creates a serious discrepancy on the value of a fundamental quantity, the proton charge radius. The current situation critically requires a possible theoretical explanation and/or the performance of a new high precision and high accuracy experiment.

With this proposal, we suggest to perform a new magnetic spectrometer free ep scattering experiment to extract the proton charge radius from the measured electric form factor G_E^p at very low Q^2 in Hall B at Jefferson Lab. We will critically improve all systematic uncertainties typical for the traditional magnetic spectrometer experiments by implementing three major improvements over previous experiments:

- (1) The extracted ep cross sections will be normalized to a well known QED process - Møller scattering.
- (2) We will reach very forward scattering angles for the first time in ep experiments while keeping the Q^2 range ($2 \cdot 10^{-4} - 2 \cdot 10^{-2}$ (GeV/c) 2) large enough for the extraction of the G_E^p slope.
- (3) The windowless, low density hydrogen gas flow target will sufficiently reduce the experimental background typical for all previous ep experiments.

With that, we will reach sub-percent precision on the differential cross sections measured for the first time in this low Q^2 range and extract the proton charge radius with unprecedented precision in electron scattering measurements. This experiment, with the requested 15 days of beam time, will have a direct impact on the “*proton charge radius crisis*” currently developing in hadronic physics.

References

- [1] H. Gao, Int. J. of Mod. Phys. E **12**, 1-40 (2003).
- [2] C.E. Hyde-Wright and K. de Jager, Annu. Rev. Nucl. Part. Sci. **54**, 217 (2004).
- [3] J. Arrington, C.D. Roberts, J.M. Zanotti, J. Phys. **G34**, S23-S52 (2007).
- [4] S.E. Kuhn, J.P. Chen, E. Leader, Prog. Part. Nucl. Phys. **63**, 1 (2009).
- [5] A. Faessler *et al.*, Phys. Rev. D **73**, 114021 (2006).
- [6] J. Friedrich, T. Walcher, Eur. Phys. J. A **17**, 607 (2003).
- [7] G.A. Miller, Phys. Rev. C **66**, 032201(R) (2002).
- [8] R. Alkofer *et al.*, Few Body Syst. **37**, 1 (2005).
- [9] A. Holl *et al.*, Nucl. Phys. A **755**, 298 (2005).
- [10] J.J. Kelly, Phys. Rev. C **66**, 065203 (2002).
- [11] M.R. Schindler, J. Gegelia, S. Scherer, Eur. Phys. J. A **26**, 1 (2005).
- [12] S. Scherer, Prog. Part. Nucl. Phys. **64**, 1 (2010).
- [13] J.D. Bratt *et al.*, Phys. Rev. D **82**, 094502 (2010).
- [14] T. Yamazaki *et al.*, Phys. Rev. D **79**, 114505 (2009).
- [15] P. Hagler, Phys. Rep. **499**, 49 (2010).
- [16] D.S. Armstrong *et al.*, Phys. Rev. Lett. **95**, 092001 (2005).
- [17] A. Acha *et al.*, Phys. Rev. Lett. **98**, 032301 (2007).
- [18] R. Pohl *et al.*, Nature **466**, 213 (2010).
- [19] P.J. Mohr, B.N. Taylor, Rev. Mod. Phys. **80**, 633 (2008).
- [20] J.C. Bernauer *et al.*, Phys. Rev. Lett. **105**, 242001 (2010).
- [21] X. Zhan *et al.*, arXiv:1102:0318 [nucl-ex] (2011).
- [22] C.B. Crawford *et al.*, Phys. Rev. Lett. **98**, 052301 (2007).
- [23] G. Ron *et al.*, to be published.
- [24] M. Paolone *et al.*, Phys. Rev. Lett. **105**, 072001 (2001).
- [25] A.J.R. Puckett *et al.*, Phys. Rev. Lett. **104**, 242301 (2010).
- [26] J. Arrington, W. Melnitchouk, and J.A. Tjon, Phys. Rev. C **76**, 035205 (2007).

- [27] I. Sick, Phys. Lett. **B576**, 62 (2003).
- [28] F. Borkowski *et al.*, Nucl. Phys. B **93**, 461 (1975).
- [29] J.J. Murphy, II, Y.M. Shin and D.M. Skopik, Phys. Rev. C **9**, 2125 (1974).
- [30] G. Ron *et al.*, Phys. Rev. Lett. **99**, 202002 (2007).
- [31] M.N. Rosenbluth, Phys. Rev. **79**, 615 (1950).
- [32] L.N. Hand, D.G. Miller, and R. Wilson, Rev. Mod. Phys. **35**, 335 (1963).
- [33] G.G. Simon *et al.*, Nucl. Phys. **A333**, 381 (1980).
- [34] M. Weitz *et al.*, Phys. Rev. Lett. **72**, 328 (1994).
- [35] E.W. Hagley and F.M. Pipkin, Phys. Rev. Lett. **72**, 1172 (1994).
- [36] D.J. Berkeland, E.A. Hinds, and M.G. Boshier, Phys. Rev. Lett. **75**, 2470 (1995).
- [37] S. Bourzeix *et al.*, Phys. Rev. Lett. **76**, 384 (1996).
- [38] A. Van Wijngaarden *et al.*, Can. Journal of Phys. **76**, 95 (1998).
- [39] B. Dudelzak, thesis, University of Paris (1965).
- [40] G. Höhler *et al.*, Nucl. Phys. **B114**, 505 (1976).
- [41] S.D. Drell and S. Fubini, Phys. Rev. **113**, 741 (1959).
- [42] G. Greenhut, Phys. Rev. **184**, 1860 (1969).
- [43] R. Rosenfelder, Phys. Lett. **B479**, 381 (2000).
- [44] R.J. Hill, G. Paz, Phys. Rev. D **82**, 113005 (2010); arXiv:1008.4619 [hep-ph] (2010).
- [45] R.G. Arnold, C.E. Carlson, F. Gross, Phys. Rev. C **23**, 363 (1981).
- [46] Jefferson Lab Experiment, E08-007, Spokespersons: J. Arrington, D. Day, D. Higinbotham, R. Gilman, G. Ron, and A. Sarty.
- [47] T.W. Donnelly, A.S. Raskin, Annals of Physics **169**, 247 (1986).
- [48] H. Gao, J. Calarco *et al.*, MIT-Bates proposal on “Precise Determination of the Proton Charge Radius (1999)”.
- [49] D. Crabb *et al.*, Phys. Rev. Lett. **64**, 2627 (1990).
- [50] C. Keith *et al.*, Nucl. Instr. and Meth. A **501**, 327 (2003).
- [51] M. Weitz *et al.*, Phys. Rev. A **52**, 2664 (1995).
- [52] C. Schwob *et al.*, Phys. Rev. Lett. **82**, 4960 (1999).

- [53] K. Melnikov and T. Ritbergen, Phys. Rev. Lett. **84**, 1673 (2000).
- [54] S.G. Karshenboim, Phys. Rep. **422**, 1 (2005).
- [55] M.A. Belushkin, H.-W. Hammer, U.-G. Meissner, Phys. Rev. C **75**, 035202 (2007).
- [56] V. Barger, C-W. Chiang, W-Y. Keung, D. Marfatia, Phys. Rev. Lett. **106**, 153001 (2011).
- [57] E. Borie, Phys. Rev. A **71**, 032508 (2005).
- [58] U.D. Jentschura, Annals of Physics **326**, 500 (2011).
- [59] C.E. Carlson, V. Nazaryan, K. Griffioen, Phys. Rev. A **83**, 042509 (2011).
- [60] R.J. Hill, G. Paz, arXiv:1103.4617 [hep-ph] (2011).
- [61] M.O. Distler, J.C. Bernauer, T. Walcher, Phys. Lett. B **696**, 343 (2011).
- [62] A. De Rújula, arXiv:1008.4546 [hep-ph] (2010).
- [63] A. De Rújula, Phys. Lett. B **693**, 555 (2010).
- [64] A. De Rújula, Phys. Lett. B **697**, 26 (2011).
- [65] I.C. Clöet, G.A. Miller, Phys. Rev. C **83**, 012201(R) (2011).
- [66] J.D. Carroll, A.W. Thomas, J. Rafelski, G.A. Miller, arXiv:1105.2384 [physics.atom-ph] (2011).
- [67] G.A. Miller, A.W. Thomas, J.D. Carroll, J. Rafelski, arXiv:1101.40732 [physics.atom-ph] (2011).
- [68] J. Arrington *et al.*, Jefferson Lab Proposal E-08-007.
(http://www.jlab.org/exp_prog/proposals/08/PR-08-007.pdf)
- [69] “A Proposal for the DarkLight Experiment at the Jefferson Laboratory Free Electron Laser”, P. Fisher *et al.*, Jefferson Lab proposal PR12-11-008, 2011.
([http://www.jlab.org/exp_prog/PACpage/PAC37/proposals/Proposals/New Proposals/PR-11-008.pdf](http://www.jlab.org/exp_prog/PACpage/PAC37/proposals/Proposals/New%20Proposals/PR-11-008.pdf))
- [70] “Technical Design Report for the OLYMPUS Experiment”, 2010.
(http://web.mit.edu/OLYMPUS/DOCUMENTS/TDR/OLYMPUS_TDR_July_2010.pdf)
- [71] D. DeSchepper *et al.*, Nucl. Instr. and Meth. A **419**, 16 (1998).
- [72] A. Roth, Vacuum Technology, North-Holland, Elsevier Sci. Publ. B.V., 3rd updated ed. (1990).
- [73] “Compact Muon Solenoid Technical Proposal”, CERN/LHCC 94-38, LHCC/P1 (1994).
- [74] K. Mengel *et al.*, IEEE Trans. Nucl. Sci. **45**, 681-685 (1998).

- [75] PrimEx Conceptual Design Report, 2000.
(<http://www.jlab.org/primex/>)
- [76] J. Appel *et al.*, Nucl. Instr. and Meth. **127**, 495 (1975).
- [77] L.C. Maximon, J.A. Tjon, Phys. Rev. C **62**, 054320 (2000).
- [78] A. Afanasev, I. Akushevich, N. Merenkov, Phys. Rev. D **64**, 113009 (2001).
- [79] I. Akushevich *et al.*, hep-ph/1104.0039.
- [80] A. Ilyichev, and V. Zykunov, Phys. Rev. D **72**, 033018 (2005).